NTNU – Trondheim
Norwegian University of
Science and Technology

Using Background OH Airglow from astronomical Observations for atmospheric Research: A Proof of Concept

Christoph Franzen

Physics
Submission date: July 2015
Supervisor: Robert Edward Hibbins, IFY
Co-supervisor: Patrick Joseph Espy, IFY

Norwegian University of Science and Technology
Department of Physics

Acknowledgement

This report was written for the course FY3900, Master thesis in Physics, as a partial fulfilment of the requirements to achieve a Master's degree at the Institute of Physics, NTNU, Norges teknisk-naturvitenskapelige universitet.

This thesis would not have been possible without the helping hand and the many suggestions from Prof. Robert Hibbins. He ensured that I was well equipped with the knowledge, ideas and necessary tools for this thesis, as well as for writing it all down. Thank you very much for this and for all the challenges, you gave me.

Secondly I want to thank Prof. Patrick J. Espy for all the tips and everything he equipped me with: ideas, books, papers and knowledge about spectra and scientific writing.

I am very thankful to Dr. A. A. Djupvik from the NOT for all explanations regarding telescopes, IRAF and spectroscopy, during my visit last autumn and via email throughout the whole year. Your tips and suggestions were often eye opening to me. I also want to thank the staff from the NOT for the warm welcome and the help during my visit.

I thank Dr. Rosmarie de Wit for her helpful suggestions throughout the thesis, the inspirations and the lovely figure 1.1.

I also want to thank all my friends, who supported me throughout the last year, who proof read my work and enjoyed breaks in the Norwegian sun with me, when possible.

Summary

The physics of the hydroxyl (OH) layer located in the Mesosphere and Lower Thermosphere (MLT) has become a focus of interest, as more and more climate models extend into this region. This is shown by the IPCC's[1] last two assessment reports. Yet, the number of precise measurements of this region is rather limited.

This work presents a way to use the by-product of astronomical spectroscopic data to measure the temperature of the OH layer. Such observational images are presented together with the challenges they present and a way to reduce the image into a clean spectrum is given. A temperature fitting method was created, where unresolved lines can also be considered.

On the examples of two nights recorded at the Nordic Optical Telescope (NOT), it is demonstrated that this method works correctly and to high accuracy. Even for integrations times as small as 10.8 s the error on the temperature is approximately only 0.5 K. The temperature development over the course of a night is measured and the temperature profile in altitude is inferred with these data. The results are tested with the HITRAN model[2], and the MSIS[3] model as well as compared with the work from Noll et al. in [4].

After this proof of concept follows a discussion of further research possible with this method. A routine is presented to fit the rotational level population N_o as well as the vibrational temperature of the OH airglow. Knowing N_o, the heating rates $^{\mathrm{d}\Theta}/_{\mathrm{d}t}$ can be calculated.

An experiment with dedicated telescope time at the NOT with the goal of measuring atmospheric waves of various frequencies is simulated in the last part of this thesis. It is shown, that this experiment is possible and will yield results with high signal to noise ratios.

Samandrag

Fysikken i OH-laget som ligg i MLT-regionen har kome meir og meir i fokus i dei siste åra, fordi fleire klimamodellar brukar dette laget. Det blei vist i dei siste to vurderingsrapportane frå IPCC[1], men talet på nøyaktige målingar er framleis lite.

Denne avhandlinga presenterer eit høve til å bruke biproduktet frå astronomiske spektroskopiske data til å måle temperaturen til OH-laget. Bilda frå desse observasjonane er presentert saman med utfordringane og løysingane av reduksjonsskritta som trengst for å lage eit reint spektrum av bildet. Ein metode for å tilpasse ein temperatur til spektrumet blei funne opp, som kan også kan bruke uløyste liner.

Med eksempeldata frå to netter frå "Nordic Optical Telescope" (NOT) blir det vist at denne metoden fungerer korrekt og svært nøyaktig. Også for integreringstider av 10,8 s, blir usikkerheita til temperaturen omtrent berre 0,5 K. Temperaturutviklinga ei natt og temperaturprofilet i høgda blir målt med desse dataa. Resultata blir testa med modellane frå HITRAN[2] og MSIS[3] og samanlikna med arbeidet frå Noll et al. i [4].

Etter denne vurderinga følgjer ein diskusjon av framtidas forsking som blir mogleg med denne metoden. Med kunnskapen om N_o kan oppvarmingshastigheita $^{\mathrm{d}\Theta}/_{\mathrm{d}t}$ reknast ut.

Eit eksperiment med tildelt observasjonstid ved NOT som hadde som mål å måle atmosfæriske bølgjer med ulike frekvensar blir simulert i den siste delen av denne avhandlinga. Det blir vist at dette eksperimentet er mogleg og vil gje resultat med høgt signal-til-støy-tilhøve.

Contents

Chapter 1

Introduction

The Intergovernmental Panel on Climate Change (IPCC)[1] published their fourth Assessment Report in 2007 with the title "an authoritative international statement of scientific understanding of climate change" [5]. Of all models used in this report, only 4 of them reached altitudes higher than 45 km; that is to say higher than the stratosphere. Only six years later, in IPCC's most recent report, the fifth Assessment Report[6], all of the highest ten models reach into the mesosphere, with one even reaching the thermosphere. In figure 1.1, the highest ten models of both reports are shown, together with a temperature profile of the atmosphere for altitudes between 0 km and 120 km.

This clearly shows how important the knowledge about this region is. There have been numerous measurements of the upper mesosphere before, in part with satellites (see for example [8] or [9]), rockets (for example [10]) or ground based spectrometers (for example [11]). Hydroxyl (OH) spectroscopy is a useful tool, as OH strongly radiates at these altitudes. See section 2.2 for further details.

For a long time, spectroscopy has been a normal tool for astronomy. The atmospheric OH radiation can be seen in near-infrared spectroscopy. These lines are seen as background effects which perturb the astronomical data. Normally, these lines are subtracted. Since many observatories save their raw data files with the atmospheric background, there is a large amount of data containing atmospheric OH radiation measurements. This thesis will demonstrate that these data can be used to obtain precise measurements of the OH airglow from background data with short integration times.

This technique is promising and can yield both historically important as well as new data from astronomical telescopes. It would also provide a new atmospheric usage for telescope data without impacting the astronomical observations. If observing time is available for dedicated atmospheric measurements, this method can be used to measure atmospheric waves, the primary vertical energy exchange mechanism in the atmosphere. This will be discussed in more detail in chapter 8.

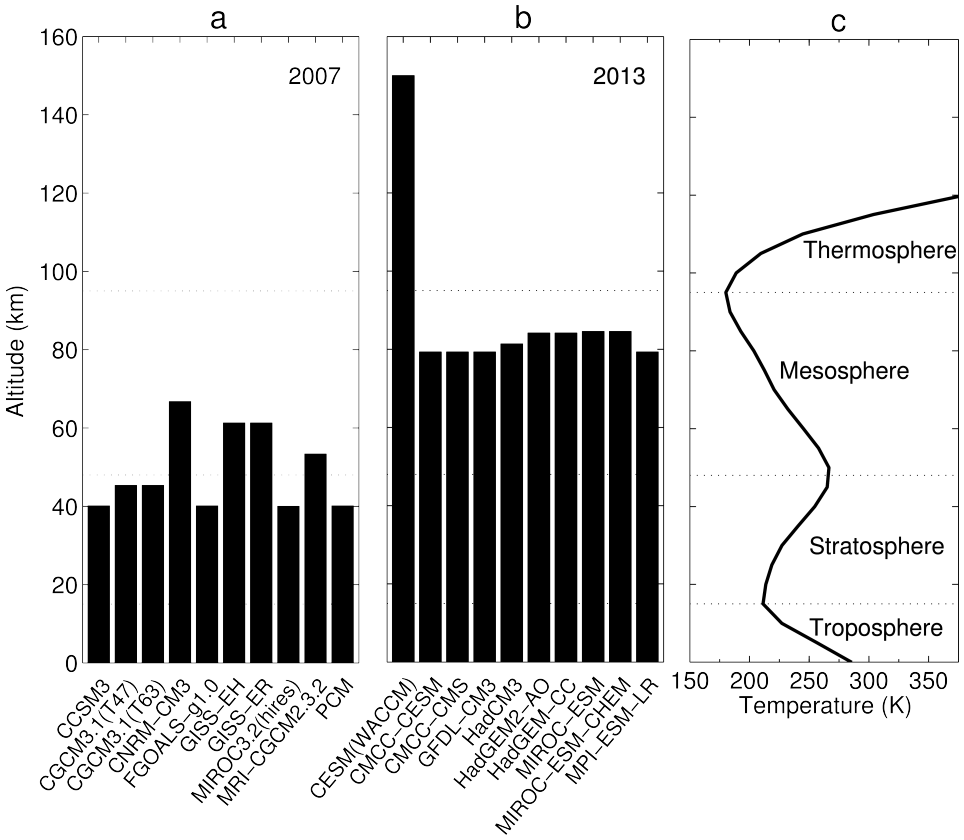

Figure 1.1: The models covering the highest altitudes from the two most recent IPCC reports [5] in (a) and [6] in (b). In (c) a temperature profile of the atmosphere at these altitudes is shown. The figure is strongly inspired from [7] and prepared by Dr. Rosmarie de Wit.

Chapter 2

Theory

2.1 The structure of the atmosphere

The atmosphere is strongly connected and in constant movement, but in the big picture, one can divide it into several layers, depending on the processes taking place there and therefore the temperature change with altitude (see also figure 2.1).

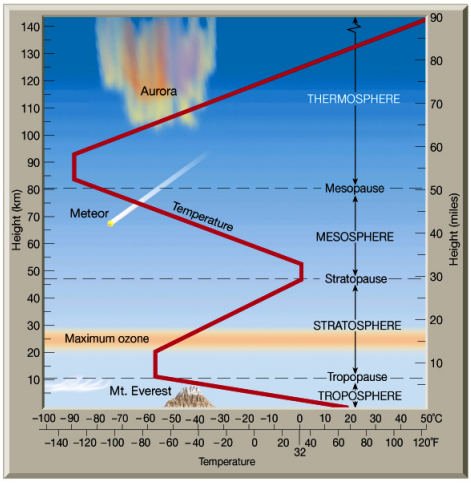

Figure 2.1: Atmospheric temperature profile as a function of height. Source: [12]

The lowest layer from the Earth's ground up until 13-15 km is called the troposphere. Here, the weather takes place. The mountain tops do not leave this layer and most normal aeroplanes fly at this hight. The temperature gradient $^{\mathrm{d}T}/_{\mathrm{d}z}$ is negative as the temperature drops with height. This is due to the transfer of the solar energy absorbed at the Earth's surface, and therefore the temperature decreases with distance to the surface. The region between around 15-20 km is called

tropopause. Here the temperature decline stops at around $-55\,^{\circ}\mathrm{C}$.

The next layer is called stratosphere and reaches to about 45 km. As seen in figure 2.1, the maximum of the ozone concentration is situated in this layer. Together with molecular oxygen, the ozone is dissociated by the ultraviolet radiation from the sun, resulting in heating of this layer. This process becomes less important with decreasing atmospheric density of the ozone. The temperature peaks locally in the stratopause, which reaches from around 45-50 km. The temperature reached again around $0\,^{\circ}\mathrm{C}$.

The mesosphere is the next layer at around 50-85 km. Here the low density means that the carbon dioxide and other infrared active molecules that are present throughout the lower atmosphere can now radiate the heat away to space. Therefore, $^{\mathrm{d}T}/_{\mathrm{d}z}$ is negative again here. The temperature drops to about $-90\,^{\circ}\mathrm{C}$. The low, decreasing density with altitude in the mesosphere means that incoming meteors encounter increased frictional heating and burn up near 90 km, leaving trace metalic elements in this region. In addition, atmospheric waves propagating up from below grow in amplitude in the decreasing density to conserve energy. Above the stratopause, the largest amplitude waves become unstable and "break", depositing their momentum and dissipating their energy. This wave energy and momentum, modulated by the seasonal winds below, drive this region from radiative equilibrium and establish a global circulation from the summer to the winter pole. The resulting uplift in summer drives additional cooling to $-140\,^{\circ}\mathrm{C}$ while the convergence and downward motion at the winter pole can raise temperatures to $-20\,^{\circ}\mathrm{C}$. As a result, the small amounts of water vapour present in the mesosphere during summer can condense and form Noctilucent Clouds (NLC) near 80 km[13].

Extending to space above the mesopause is the thermosphere. This layer is heated by the extreme ultraviolet sunlight directly. As the density is very low, the heat content does not become very high, even though the temperatures goes up to $800\,^{\circ}\mathrm{C}$ or even $1{,}200\,^{\circ}\mathrm{C}$ depending upon the solar cycle. A known phenomenon taking place in the thermosphere are the northern lights.

The transition region in the atmosphere between the thermosphere and the neutral middle atmosphere, called the Mesosphere and Lower Thermosphere (MLT), is both chemically and dynamically highly variable [14, 15]. It is driven from above by diurnal, seasonal and long-term changes in solar radiation and from below by tides, planetary waves and upward propagating gravity waves. The MLT region will be the focus of this work, as the hydroxyl layer (see as well section 2.2) is situated here.

Of course, all the numbers presented above are averages, as the temperature is dependent on the latitude, of the part of the atmosphere concerned, as well as season and local weather.

The UN Committee on Space Research (COSPAR) has assembled an empirical model reference atmosphere CIRA[16, 17] (COSPAR International Reference Atmosphere) that is hosted by the Community Coordinated Modelling Centre (CCMC[18]) at NASA.

The model can be found as a ASCII version at: `ftp://hanna.ccmc.gsfc.nasa.gov/pub/modelweb/atmospheric/cira/cira86ascii/nht.lsn`. In figure 2.2, the

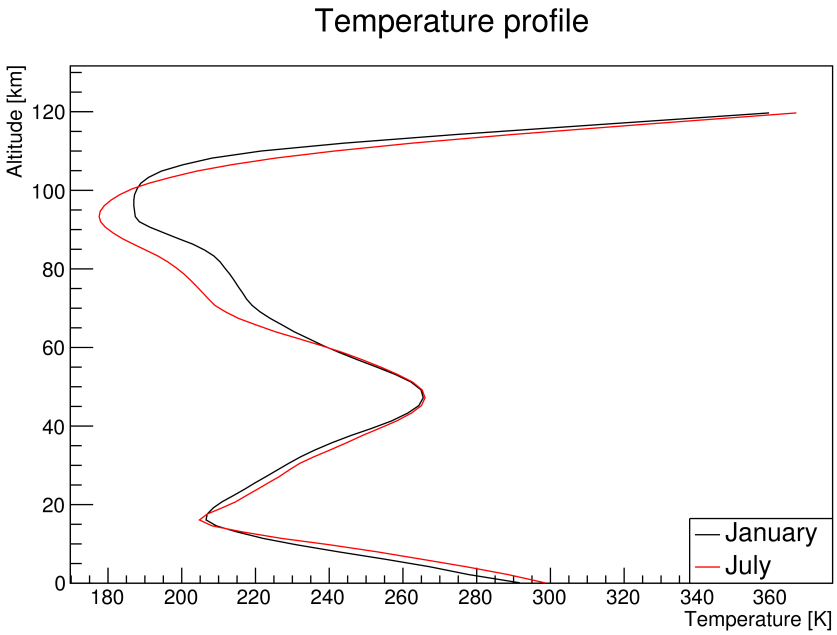

Figure 2.2: Temperature profiles of the atmosphere at latitude 30 °N created with the CIRA86 data for January and July. The biggest deviations can be observed in the mesosphere and MLT region.

mean model values are plotted for the month January and July for a latitude of 30 °N, where the data for this thesis were taken[1]. One can see that the largest deviation between the two temperature profiles is in the mesosphere and the MLT region. Temperatures lower than 175 K are not expected in these models. A similar model, the MSIS model, from the CCMC will be used later in section 7.3.

2.2 The layer of excited hydroxyl

Around the mesopause region photochemical reactions play a key role in the production of chemi-luminescence that is observed as the night airglow. One such process is the reduction of ozone to molecular oxygen[19]:

$$H + O_3 \rightarrow OH^* + O_2 \tag{2.1}$$

However, the ozone is naturally mostly formed during the night by the combination of molecular and atomic oxygen via a mediator M:

$$O + O_2 + M \rightarrow O_3 + M, \tag{2.2}$$

[1] See as well chapter 3 Instrumentation.

Here, the atomic oxygen is formed by photo-dissociation of molecular oxygen [20, 21] and the ozone during daytime, and peaks near 95 km.

The production rate P_{OH^*} can be calculated to be

$$P_{OH^*} = k_{H+O_3}[H][O_3] \tag{2.3}$$

However, since the reaction producing the OH* is also the primary loss reaction of ozone during the night, the ozone concentration can be derived from equation 2.2, using the balance between loss and production:

$$[O_3] = \frac{k_{O+O_2+M}[O][O_2][M]}{k_{O_3+H}[H]} \tag{2.4}$$

Thus the production rate of the vibrationally excited OH* that radiates in the airglow becomes:

$$P_{OH^*} = k_{O+O_2+M}[O][O_2][M] \tag{2.5}$$

The OH^* production is the product of atomic oxygen, which increases to a peak value at 95 km, and the molecular O_2 and M species that decay exponentially with altitude. This forms a thin layer of OH at night, with the highest OH^* concentration at 87 ± 3 km and the half width of the layer is 7 ± 3 km[22].

As the ozone is rapidly dissociated by sunlight, its concentration rises rapidly after sundown by equation 2.2. As its concentration rises, it does so at the expense of the atomic oxygen that limits its growth. At the same time, it is destroyed through reaction 2.1 to form the OH^*, which eventually reduces the O_3 concentration during the night. Since the concentration of atomic hydrogen is nearly constant during the night, the vibrationally excited hydroxyl tracks the ozone concentration, reaching a peak value after sunset and decaying during the night. However, the concentration does not follow a simple exponential decay law, but is perturbed by gravity waves, tides and atmospheric perturbations. Due to transport of atomic oxygen from the dayside, a rise of the concentration shortly before sunrise is not unusual as well. This can be seen in figure 2.3, from [23]. There, a typical night development is shown, including the increase shortly before dawn. However, the night sky and the OH airglow is highly variable, as observed from Parihar et al. [24] and many others.

2.3 OH spectroscopy

From Earth, the reaction 2.1 is only visible by the radiation from the OH^*. Therefore, it is important to know how the temperature and the concentration of OH^* changes the OH airglow.

Deactivation of the high vibrational states of the products from equation 2.1 occurs primarily through photo-emission in the Meinel bands of airglow [25] which are observed in the red and near infrared part of the electromagnetic spectrum. The two body problem of an exited OH molecule can be solved with the help of quantum mechanics. A good overview of this can be found in several textbooks, for example in [26].

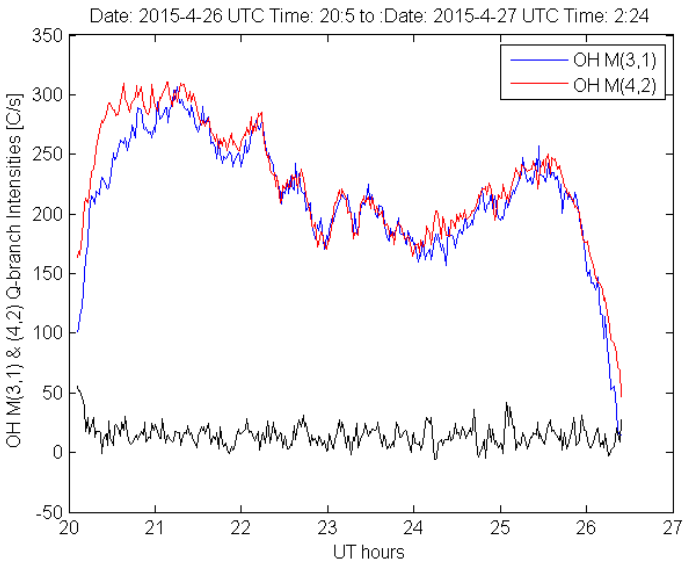

Figure 2.3: A typical nightly development of the OH airglow intensity. The red and the blue line are two different Meinel bands, whereas the black line is from an Na doublet, which appears near 1.66 μm and is reflected from the clouds and thus was used as a cloud detector. As this value is constantly low, it can be seen that this was a cloudless night. Source [23]

.

2.3.1 Line intensity

Due to the different masses of electrons and nuclei, as well as the higher restoring forces for molecular vibration, the energy of the system can be split into three parts:

$$E = E_e + E_v + E_r \tag{2.6}$$

For transitions within the same electronic orbital configuration, E_e is the total binding energy of the electrons to the nuclei, E_v is the vibrational energy and E_r is the rotational energy. These are straightforward to calculate when separated from the others for a simple diatomic molecule as OH. The results are quantum mechanically separated energy levels labelled by their quantum numbers (v for vibration and J for rotation).

Since this problem is well established for the OH molecule, a database will be used for the OH lines. The HITRAN[2] database maintains an up-to-date list of all important transition lines, calculated to high precision. From there, one achieves for each transition between specified vibrational-rotational levels for the OH molecule:

- ν: vacuum wavenumber of the transition in cm^{-1}

- $A_{u\to l}$: Einstein A coefficient for a given transition between upper state u and lower state l in s^{-1}
- E_l: lower-state energy in cm^{-1}
- g_u: statistical weight of the upper state

The energy of the upper state is then simply $E_u = E_l + \nu$. From here, the emission intensity from an upper state is given by:

$$I_{u\to l} = N_o g_u e^{-\frac{E_u}{k_B T}} A_{u\to l} \tag{2.7}$$

Where N_o is the total OH^* density. Multiplying this by the degeneracy and the exponential factor gives the number of molecules in the upper state. k_B is the Boltzmann constant, in these units $k_B = 0.695{,}035{,}612\,\frac{\mathrm{cm}^{-1}}{\mathrm{K}}$, where the last 2 digits are uncertain.

The intensity 2.7 is then divided by the partition function of all upper states u_i:

$$Q = \sum_{u_i} \left(1 + g_{u_i} e^{-\frac{E_{u_i}}{k_B T}}\right) \tag{2.8}$$

That is:

$$I_{u\to l} = \frac{N_o g_u}{Q} e^{-\frac{E_u}{k_B T}} A_{u\to l} \tag{2.9}$$

The energy diagram for the OH model can be found in figure 2.4 with the transitions between the different rotational and vibrational states labelled. A sample spectral distribution created using equation 2.9 is shown in figure 2.5 with the most prominent transitions labelled. The Q-branch[25], seen in figure 2.4 to arise from vibrational transitions with no change in the rotational quantum number ($\Delta J = 0$), is situated near the center of the transition's spectral region in figure 2.5.

On the left hand side of the Q-branch is the R-branch, drawn in green. This branch comes from transitions with $\Delta J = +1$. Due to the higher energy of the second sub-state, the R_2 lines are less intense. As this branch is of very low intensity in comparison to the Q-branch, these lines are easily perturbed by noise and will therefore be of less use than the other lines.

The branch on the right hand side of the Q-branch, shown in figure 2.5 is called the P-branch, plotted in blue. This branch originates in transitions with $\Delta J = -1$. The P-branch is divided in the same way as the R-branch.

2.3.2 Temperature dependency

The population of the rotational states of each long-lived vibrational excited state follows Boltzmann statistics. Hence high spectral resolution spectroscopic measurements of the relative population of the rotational levels in each vibrational

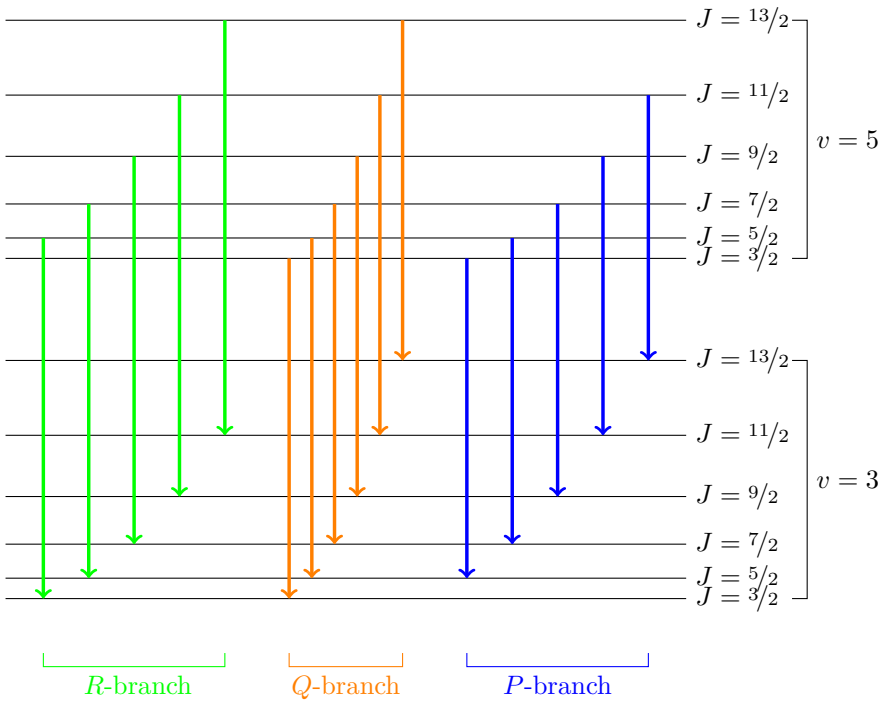

Figure 2.4: Energy level diagram of the OH molecule. In the colours, green, orange and blue, the three branches are shown. In figure 2.5, the corresponding branches are shown in the same colour. This energy level diagram is for the $F_1 = 3/2$ spin electronic sub-state that gives rise to the P_1, Q and R_1 sequence. An identical energy manifold at slightly higher energy would exist for the $F_2 = 1/2$ sub-state, with the higher energies accounting for their reduced intensity.

band can be used to remotely sense the rotational temperature of the mesopause region.

In figure 2.6, three variations of the 5-3 transition (as in figure 2.5) are plotted, each with a different rotational temperature. Here, all the transitions were normalized that the $Q(1)$ line has an intensity of 1 in arbitrary units. One can see, that then also the $P_1(1)$ lines are of the same intensity for different rotational temperatures. This temperature dependency will be used later on to find the temperature of a recorded transition. See as well chapter 5.

The high rotational levels of OH, where the energy spacing is greater than the typical energy quantum exchanged by collisions, kT, do not thermalize rapidly[27]. Following Cosby and Slanger[28], only lines originating from levels $N \leq 4$ have been considered for the temperature fitting. This is not a significant loss of data, since the $N = 5$ levels mostly overlap with the R-branch of the neighbouring transition. For further details on line selection and overlap of the transitions, see chapter 5.

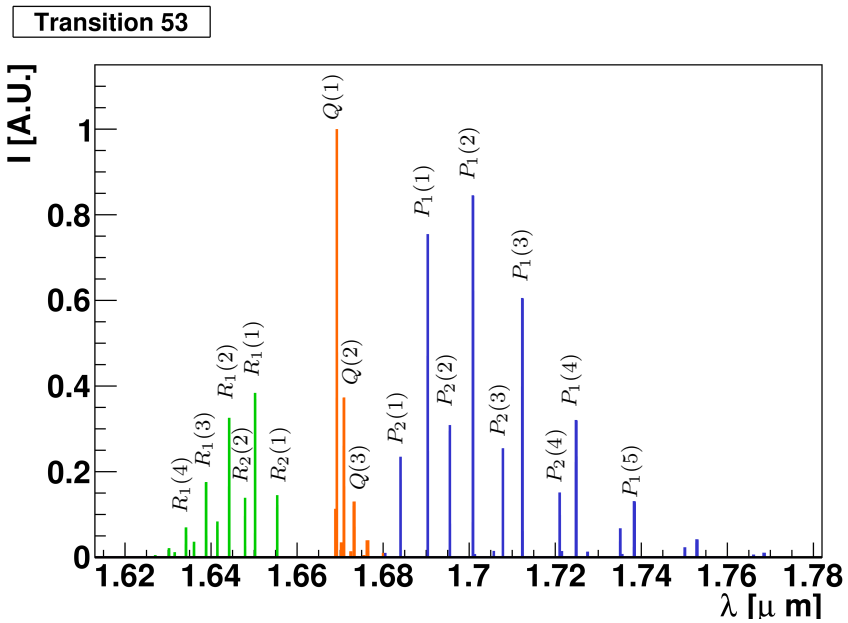

Figure 2.5: Model spectrum of the transition $v' = 5$ to $v = 3$ created with HITRAN[2] data with a temperature of 200 K. The intensity of the OH airglow is in arbitrary units. The most prominent lines are named. The spectrum is clean, thus the lines were not broadened in any way or perturbed with noise.

2.3.3 Concentration of excited OH

Reaction 2.1 is highly exothermic (> 3 eV) leading to population of the vibrational levels from v'=7 to v'=9 of the OH product. This energy will then cascade down the vibrational manifold through Meinel band transitions and quenching, and can transfer heat from the dissociation from molecular oxygen in the lower Thermosphere into the Mesopause region[29].

The concentration of OH in a given vibrational level in the mesopause region is given by:

$$[\mathrm{OH}(v)] = \frac{f_v P_C \sum_{v'} A_{v'\to v}[\mathrm{OH}_{v'}] \sum_{v'} k_{v'\to v}[\mathrm{M}][\mathrm{OH}_{v'}]}{\sum_{v'} A_{v'\to v} \sum_{v'} k_{v'\to v}[\mathrm{M}] + k'_c[\mathrm{O}]} \tag{2.10}$$

where P_C is the production rate of vibrational excited OH (reaction (2.5)) and f_v is the fraction of production into state v. The other two terms in the numerator describe indirect sources of OH(v): spontaneous emission, and collisional deactivation processes ($k_{v'\to v}$ is the quenching rate) from vibrational states with higher vibrational energy. The denominator consists of radiative, collisional and chemical loss mechanisms.

The heat deposited by the H + O_3 reaction can be derived directly from the [OH(v)] measurements if the number density of at least one vibrational mode of

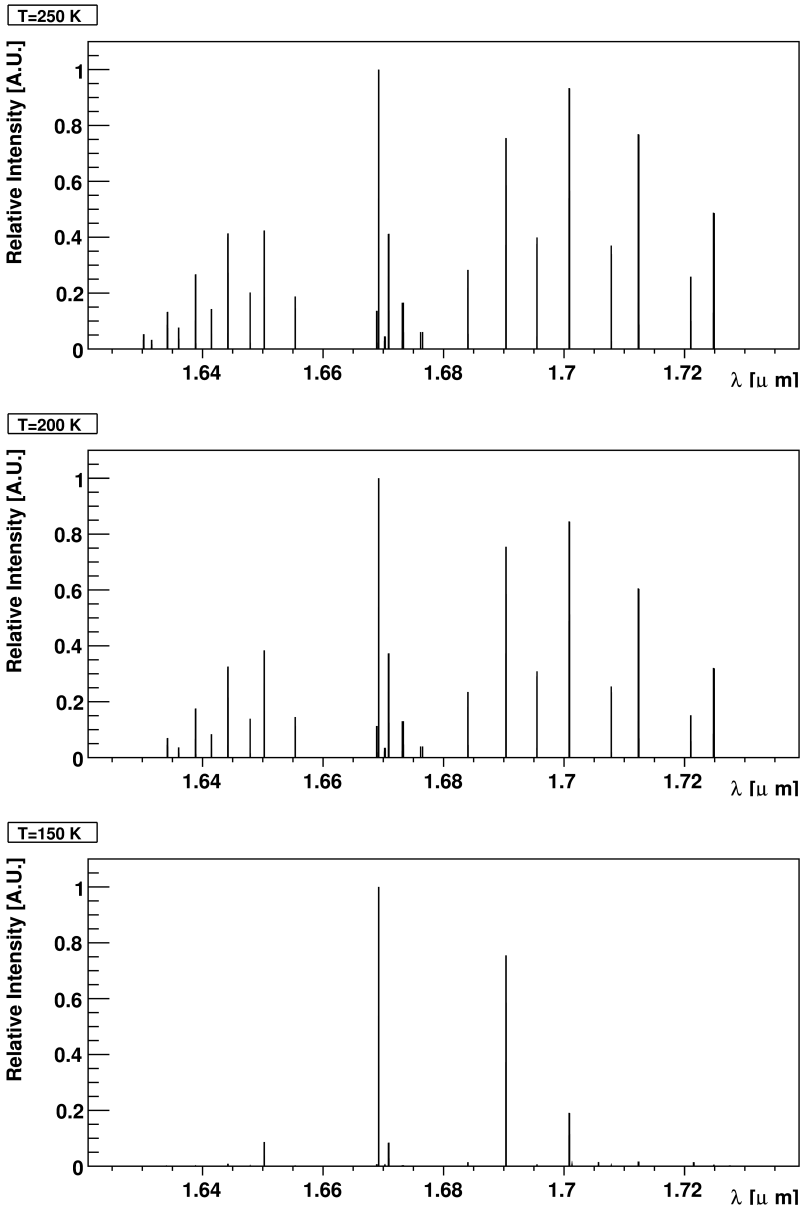

Figure 2.6: Model of the 5-3 transition as in figure 2.5, but this time with three different temperatures. The line intensities are clearly influenced by the temperature, as already seen in equation 2.9. All three transitions were normalized that the $Q1(1)$ line has intensity of one.

OH and all its productions and losses are known. Equation 2.10 is simplified if one considers the highest vibrational state populated in the $OH^{\star}$ formation reaction ($v = 9$) because the production of this vibrational state is dependent primarily on the $H + O_3$ reaction and not from radiation or quenching cascade from higher vibrational states. Thus it is not sensitive to the choice of quenching model used (step-wise or sudden-death)[30].

The OH Meinel 9-7 transition is the brightest from the $v' = 9$ level. However, it occurs at wavelengths near $2\,\mu$m that are not easily accessible for conventional airglow instruments that typically use InGaAs detectors that are only sensitive to $1.7\,\mu$m. However, the NOTCam records Meinel spectra to beyond $2\,\mu$m and is able to measure these high vibrational bands. Hence measurements of the concentration of the $v' = 9$ vibrational level of OH^{*} in the mesopause (and how it varies with time) can be used to measure the heating rates ($^{d\Theta}/_{dt}$) due to the primary chemical heating reaction in the mesopause region using the techniques outlined in[31].

A comprehensive review on ground based observations of OH and their applications to mesopause chemistry can be found in [11] [32], [33] and [34].

Chapter 3

Instrumentation

Founded in 1984, and located on La Palma ($17^\circ\,53'\,06.3''$ W, $+28^\circ\,45'\,26.2''$), the Nordic Optical Telescope (NOT) has a primary mirror with a diameter of 2,560 mm. For near-infrared imaging and intermediate dispersion spectroscopy, the NOTCam has been in operation since the 30th of June 2001[35]. This instrument is based on a 1,024×1,024 pixel Rockwell Science Center HgCdTe "HAWAII" array. It is assembled from four subarrays.

Two spectral resolutions are possible, low (R =2,500) and intermediate (R =5,500). The low resolution mode is sufficient to resolve most of the individual rotational lines of a given OH vibrational level. The spectrum is taken with the help of a grism. In the low resolution spectroscopic mode the employed slit has a width of 128 μm corresponding to approx. $0.6''$[35] and a slit length of $4'$. At an approximate OH layer altitude of 87 km [22] $4'$ correspond to around 100 m on the sky. The gain is approximately $2.5\,{}^{e^-}/_{\text{count}}$[36]. Further details on the NOTCam can be found in [35].

The NOTCam is only one of the imaging instruments of the NOT. The full list with a short description of all the instruments can be found in table 3.1, found at [35]. Since the change between instruments takes time and not all instruments are used for all experiments done at the NOT, the NOTCam was not mounted continuously in the past. In figure 3.1, the nights where the NOTCam was used between 2007 and 2014 are shown. Here the day of the month is on the x-axis and the month on the y-axis. One can see that no particular periods are overly represented and a good sampling can be achieved for long-term evaluation of NOTCam images.

The spectroscopic mode has been continuous and stable with no change of optical elements, except for the addition of the two broad-band filters Z and Y in 2010. NOTCam is kept cold all the time, also during storage when not mounted on the telescope. Since about 2007 it has only been necessary to open the instrument for vacuum maintenance and installation of optical elements, less than once per year. There has been a change of detector in this period, but each array is well characterized.

During standard astronomical observations, measurements in the H, J and K band are typically taken. Atmospheric OH vibrational bands transitions 3-1, 4-2,

Instruments name	Short description
ALFOSC	UV-optical imaging, polarimetry and low-resolution spectroscopy
NOTCam	NIR imaging, polarimetry and low-resolution spectroscopy
FIES	High-resolution, high-stability optical spectroscopy
MOSCA	High-resolution, high-efficiency UV-optical imaging
StanCam	Standby CCD imager

Table 3.1: The full list of imaging instruments at the NOT with a short description, found at [35]

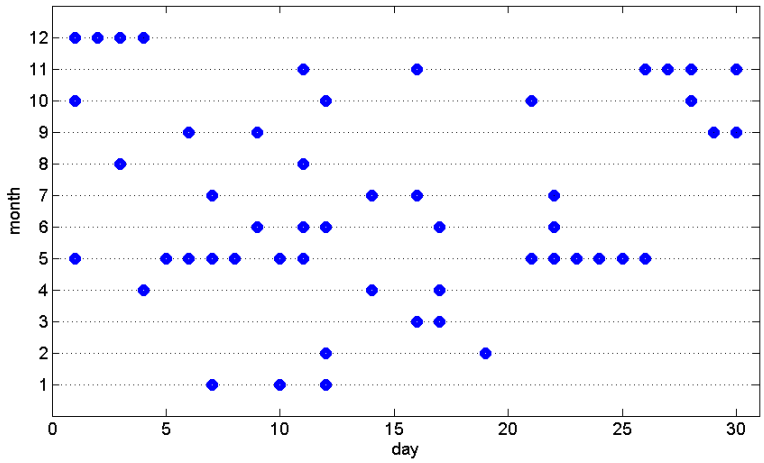

Figure 3.1: Dates between November 2007 and March 2014 when the NOTCam has been mounted at the NOT and making spectroscopic astronomical observations.

5-3 and a part of 6-4 are simultaneously observed in the H band, 7-4 and 8-5 in the J band and finally the 8-6 and 9-7 in the K band [25]. The 9-7 transition is specifically of interest as it represents the highest vibrational level populated by the exothermic reaction 2.1. As every level from $v' = 9$ to $v' = 3$ is in one of these bands, the whole cascade from $v' = 9$ down to $v = 1$ can be observed.

The filter characteristics for H, J and K band filters used by the NOTCam can be found in figure 3.2. The non-flat plateau and the finite rising and falling edges have to be corrected for. This is done during the flat-fielding operation described in detail in Chapter 5.

For a normal observation all images of the object are taken four times in a so called ABBA scheme, where the image of the object is placed on two different places A and B on the imaging array. A is situated a little to the left of the middle of the array and B a little to the right of the middle.

Each image of the ABBA scheme has the full integration time (for the obser-

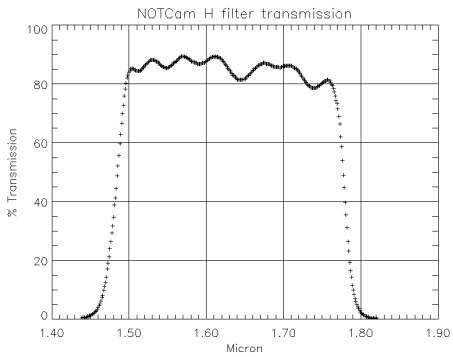

(a) Filter for the H band

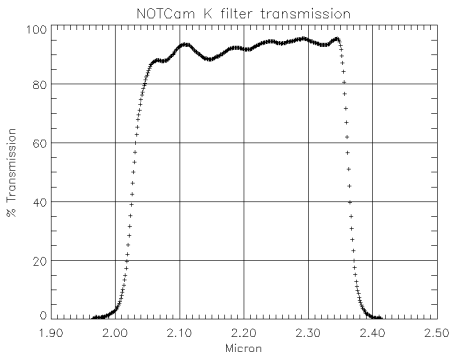

(b) Filter for the K band

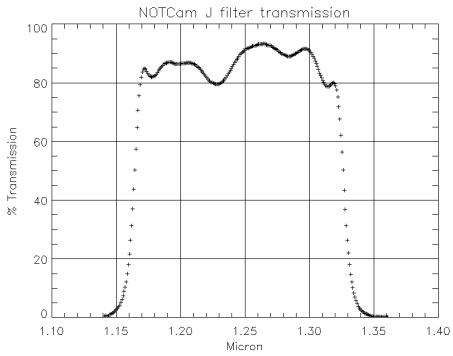

(c) Filter for the J band

Figure 3.2: Characteristics of the filters installed in NOTCam from [35]. On the x axis, the wavelength λ in μm is shown, on the y axis the transmission in %. None of the filters is completely flat. Their characteristics will be cancelled during flatfielding in chapter 5.

vation NCwb19 10.8 s). Between the images of the ABBA scheme, the NOTCam has a 10 s downtime. The star moves during the time, the ABBA scheme takes. It is tracked by the NOT. Therefore, the OH^* airglow comes from partially different parts of the sky. The distance, the star moves on the night sky is dependent on the position of the star at observation time. This effect will not be considered in this thesis, even though the observed patch of the OH^* airglow can be up to 0.5 km big. For further research, this has to be considered.

The reason for the ABBA scheme lies in the astronomical experiments. By subtracting a picture from position A from a picture from position B, the background atmospheric lines can be cancelled out. Of course, this will not be done in this work, as the background is the object of interest here. There are two images of the A and B possitions for redundancy. From experience, the first picture of the four is often perturbed by memory effects from earlier experiments. This memory effect lies at about 0.5 %[36]. In this thesis, the four images serve (if they are not damaged) as statistical verification of the data, since they are taken shortly after each other.

Aside from the experiment images, a sequence of secondary pictures are taken. These are dark (detector background) images (normally the ceiling of the telescope

dome) and images of different discharge lamps. The pictures of a halogen lamp are used for detection of filter characteristics (see also flatfielding in chapter 5). The pictures of other lamps are normally used for wavelength calibration. This was not necessary for this thesis. Though, the time it takes to take these images lessens the number of observations per hour. Therefore the number of images taken per night differs.

Chapter 4

Reduction challenges

4.1 Imaging and noise

Each element of the array detector is first electrictronically reset to a starting value, typically around 6,000 counts, and this starting frame, called the reset frame, is saved in the image file. The detector is then exposed for an integration time, t. For the images used in this work, the image is not taken in one long integration time, t, but in n frames of integration time t/n, where the individual frames are a non-destructive readout. Using this ramp-sampling mode decreases the noise on the flux rate by a factor $\sqrt{n}$[37]. For example, a 10.8 s integration is generally stored as three frames with net integration times of 3.6 s, 7.2 s and 10.8 s, where each stored frame has the reset frame subtracted from it. The final, top-level frame is then the linear regression of these intermediate integration times that provides a mean flux rate for each pixel. This final frame will hereafter be referred to simply as the image in this thesis.

From experience it takes around 10 s to read out the data after an integration. This time is not accounted for in the integration time, meaning that it takes 20.8 s to take an image with 10.8 s integration time.

There are many sources for noise expected and known for the NOTCam. Beside purely statistical noise that would go with a square root function $f(t) = p_0\sqrt{t}$ with integration time t, there are a few effects adding a constant error. The readout noise is known to be small at around 8 e^-, so approximately 3 counts[36].

Other effects that add up to a constant noise are described in section 4.2. These effects underlie a strong variation from image to image as well as from night to night.

4.2 Instrument specific effects

As mentioned before, there are a few effects that are typical for the NOTCam and that will perturb the data. A short overview over these effects will be given here. In chapter 5, how these are handled is described.

Most of these effects can be seen in figure 4.1, where the 10.8 s integration of the H band from the 19.02.2013 is shown. This is the second position A measurement from the ABBA scheme.

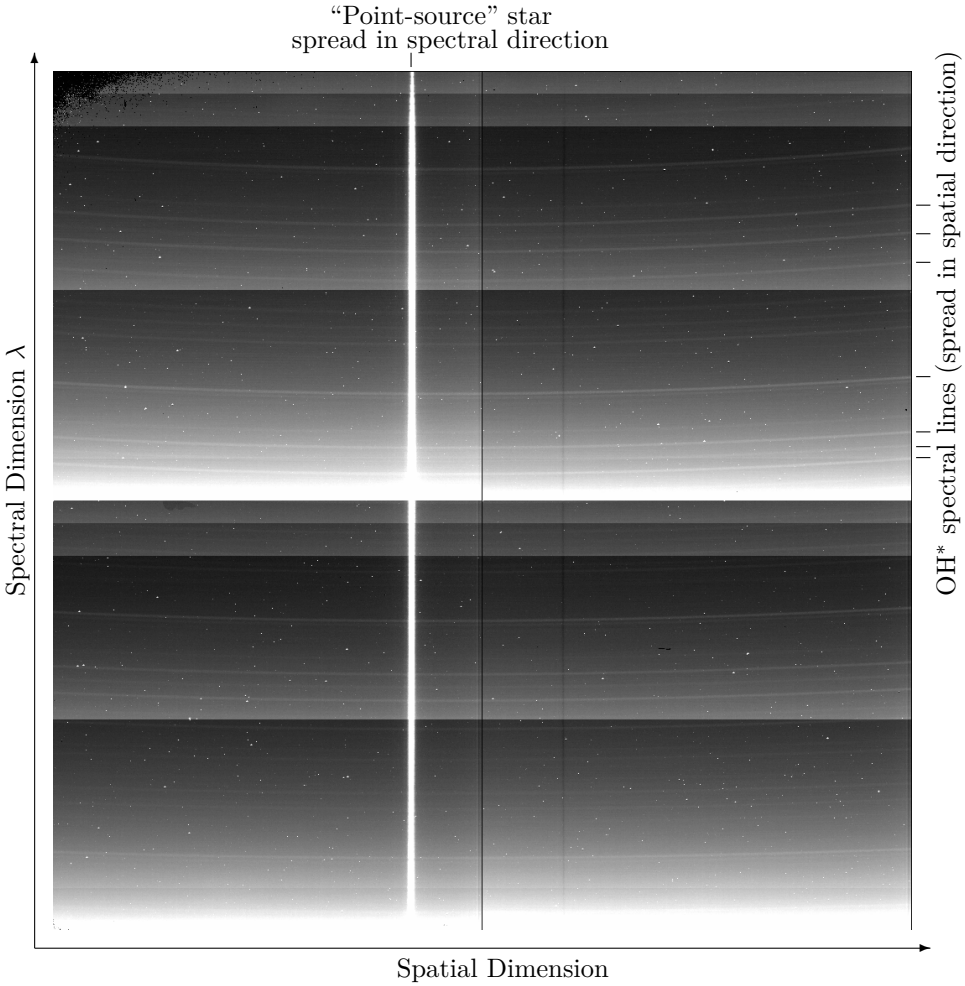

Figure 4.1: Measurement in the H band from the 19.02.2013 taken by NOTCam. The vertical bright line, a little left from the centre, is the spectrum of the star. The upwards curved lines in the background are the atmospheric lines. These are mostly OH airglow lines that will be further investigated.

For the nightglow observations, the first perturbing effect that can be seen is the presence of the star, the original object of the measurement. It can be seen as bright vertical line a little left to the middle (at position A). The star is not confined to a single line, but stretches out over approximately 60 pixels. These pixels will be eliminated from the nighglow analysis as detailed in Chapter 5.

Background steps The most obvious background effect in figure 4.1 is the slowly rising background levels progressing downwards in the image that sharply go down several times in the image. These are readout effects, as a constant signal is adding up on top of the actual signal. Further complicating the analysis is the fact that the resets do not always occur at the same positions.

Transition between subarrays As the array is composed of four subarrays, the boundaries may cause problems. Each subarray can have its own background level, and the pixels at the transition points cannot be used. They have to be excluded from the data as well.

Hot and dead pixels and cosmic rays A few white dots can be seen in figure 4.1. These are hot or dead pixels, but can also arise through cosmic rays impacts. Dead pixels give no signal at all. For hot pixels, the signal is too high. While the positions of the hot and dead pixels are known, the positions of the cosmic rays are not. Their number and position change from image to image.

Fringes These cannot be seen very well in figure 4.1, as this effect is weak in comparison to the background steps. They are however visible in some flat-field-images. Fringes are concentric circles around the middle of the array, coming from scattering of the photons within the array. However, since the OH lines (the bowed horizontal lines in Figure 4.1) cover the full spatial extent of the detector, they intersect many of these fringes. Thus, the fringe pattern will average out after integrating along each OH line, and this effect is not important for the nightglow analysis. This effect is mentioned since it is of greater importance for astronomical experiments. This is because the spatial width (the horizontal direction in Figure 4.1) of the nearly point-object star covers only a few pixels, over which the fringe pattern is relatively constant. Thus each spectral element of the star line will be offset by varying fringe pattern.

Chapter 5

Data Reduction

5.1 Reduction solutions

5.1.1 Reduction of the array

As a demonstration of the data reduction procedures H-band data taken on the night of 19th of February 2013 were used. In particular a typical standard star observation towards the star HIP61318 A1 with an exposure time of 10.8 s (3×3.6 s) was analysed. This image was taken in good astronomical observing conditions at an air mass of 1.516 at 05:50:35.5 UT, together with dark frames and flat fields recorded with a halogen lamp on the same night.

The raw image frame was already presented in figure 4.1. The vertical bright line, a little left from the centre in figure 4.1, is the H-band spectrum of the star as the star is positioned a little off from centre on the detector. The near horizontal lines, gently curved upwards, in the background are the atmospheric OH lines from the 3-1, 4-2, 5-3 and (part of the) 6-4 vibrational transitions from bottom to top in the image frame.

For the initial data reduction steps standard IRAF[38] astronomical procedures were followed. Dead and hot detector pixels are known and stable[37] and were removed, and dark frames were used to create a pixel mask to remove hot pixels on the detector. The intensity of the OH lines are well within the linear range of the detector array[37], so non-linearity effects could be neglected. The dark current was removed and the vignetting effects from the filter and optics are accounted for by flat fielding using short[1] exposure measurements of a halogen lamp.

As the star's spectrum is much brighter than the OH lines, it has to be removed. A linear mask, 60 pixels wide was applied to the detector frame centred on the star's horizontal position on the detector. 60 pixels were found to be optimal between removing all stellar influence while maintaining as much OH data as possible.

Randomly occurring cosmic ray hits on the array can be easily detected, as their number is very small in comparison to the number of pixels on the array. Thereby,

[1] In this case was the exposure time 7 s

if one pixel is at least ten times more intense than the average of the array at this point of the reduction steps, it is ignored as a cosmic ray. For the datasets used here, around 1,000 pixels were found to be contaminated by cosmic ray strikes and set to not a number (NAN). This means that statistically, approximately one pixel per row of data is eliminated.

5.1.2 Projection curvature

The atmospheric lines, which are mostly OH airglow lines, can already be seen in figure 4.1 as slightly bending upwards lines. While the lines are projected as straight lines by the grism (by normal diffraction law), the optics afterwards bends them. However, this bending is the same for all images taken with the NOTCam.

In theory, the lines should approximately follow an ellipse[35]. Since bending of the lines is small, the elliptical function is approximated by a Taylor's series expansion of second order. With this assumption, a mapping can be produced from a coordinate system (x, y), where the lines would be linear, to the original coordinate system (x', y'), where the lines are approximately parabolic. Here, $x = x'$ holds, and $y = f(x, y')$ follows the Taylor expansion with three parameters. A rewriting to $y = p_0 + (x - p_1)^2 \cdot p_2$ yields a better understanding of the parameters. The offset, p_0 is easy recognized as y'. The central position of the parabola is constant at the pixel number 465 from the left edge, between the star's aperture and the centre of the array. The curvature p_2 on the other hand is not thought to be (or found to be) constant, but dependent on the vertical position (x) on the array. This dependency can be treated as a Taylor expansion as well, this time of first order and is experimentally found to be $p_2(y') = 3 \times 10^{-5} + 5.3 \times 10^{-8} \cdot y'$.

Given this transformation, the OH lines can subsequently be summed up to form a 2D spectrum, by summing all values in x for a given y (after accounting for the pixels masked out as described above). The statistical standard deviation of the values with same y is calculated and serves as uncertainty in the following work. Using this transformation, figure 5.1 was created. One can see the same measurement from figure 4.1, but this time after all steps described so far. Only the parts with OH lines are shown. The known dead and hot pixels and the cosmic rays are shown as white spots here.

5.2 Reduction of the spectrum

5.2.1 Net line broadening

The atmospheric lines are in theory Doppler broadened. Furthermore, the optics inside the NOT and NOTCam broaden the OH airglow lines. The latter effect is measured to be much larger. Therefore, the Doppler broadening can be neglected in the analysis.

It is found that the lines on the raw data image are Gaussian to the degree of noise and have a σ value of 1 pixel. However, the flattening of the OH lines as described above can only be accurate to the scale of single pixels. Therefore, when

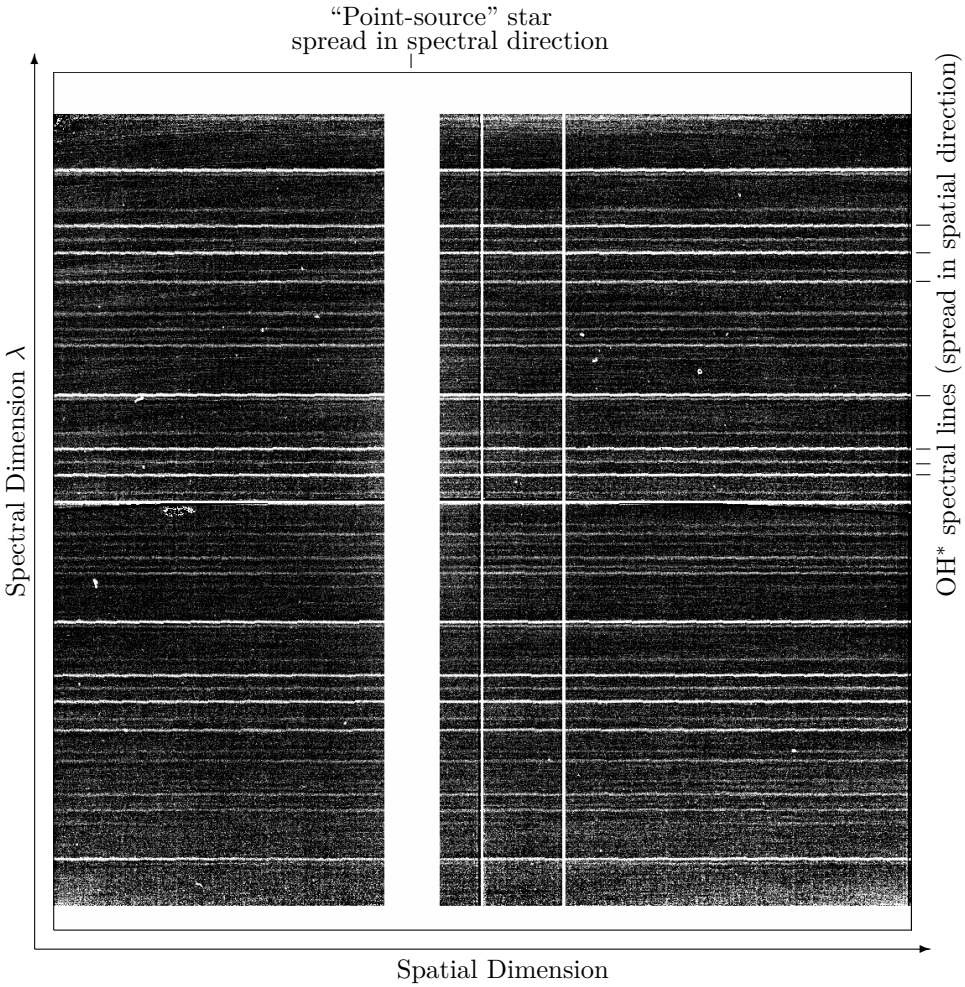

Figure 5.1: Cleaned measurement in the H band from the 19.02.2013 taken by NOTCam. Only the usable parts are shown. The star is blanked out, as well as the pixels of the transition between the four subpanels of the array, the filter verges and the bottommost 30 pixels, that cannot be straightened. The known dead and hot pixels are imaged as white dots. Visible OH lines vibrational transitions from bottom to top: 3-1, 4-2, 5-3 and (part of the) 6-4.

later on adding all the columns of the image up to achieve a normal spectrum, many Gaussian line shapes are superposed. Each of the lines shapes has σ of 1 pixel, but the centres differ on the same scale. This yields a slightly different line shape and a further broadened line. This line shape is equal to a gaussian line shape with a 4 % broader width. The actual line shape and the this gaussian line shape differ only in 0.03 % of the maximal peak hight. The new width is approximately 0.31 nm. This new line shape and width will be used in the fitting analysis.

The resulting intensity as a function of wavelength of the nightglow spectrum is then normalized to a zenith intensity by using the air mass recorded by the NOT-Cam. The air mass is given as a wavelength independent number. The uncertainty on this parameter is not directly given but the number is given with three significant figures. The air masses from the different datasets used in the thesis can be found in table 6.1.

5.2.2 Wavelength Calibration

The calibration of the spectrum from pixel number to wavelength can be done using standard measurements of the calibration lamps, where both xenon and argon lamp measurements are available. However, as the wavelengths of the OH lines are known [2] and the lines are easy to identify, the abundant lines themselves can be used for wavelength calibration. By using this technique, we avoid possible error sources from changes between the astronomical observation and the calibration measurement. If available, the highest line of the Q-branch and the six highest P-branch lines of each transition in the spectrum have been used for this. For the example presented here in the H band, this leads to a calibration based on 22 pixel/wavelength pairs (for the 6-4 transition, only the main Q-branch line was used). The calibration transformation is mostly linear with only small nonlinear contributions.

The calibration fit is shown in figure 5.2. The fitted calibration function is a polynomial of third order $f(x) = p_0 + p_1 x + p_2 x^2 + p_3 x^3$. The fitted parameters p_0 to p_3 can be found in table 5.1. The parameters for the nonlinearity p_2 and p_3 are very small and have a large error bar of around 10 %. This shows that the calibration is mostly linear.

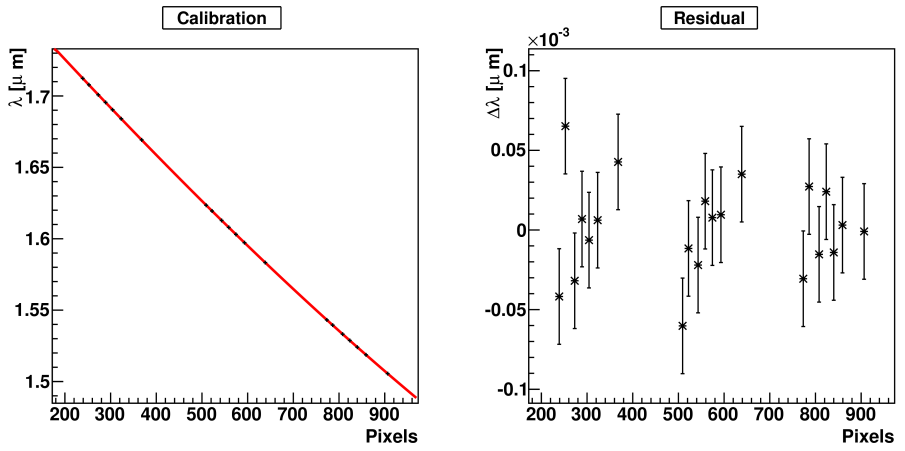

Figure 5.2: Fit for the calibration. Left, the fit of the polynomial of third order is shown through the chosen peak positions. The small error bars are shown in both panels. On the right side, the residual of the fit is shown.

With this (approximatly linear) wavelength calibration, one pixel translates approximately to 0.3 nm.

Parameter name	Value in μm	Error on the value in μm
p_0	1.795	1.966×10^{-4}
p_1	-3.551×10^{-4}	1.249×10^{-6}
p_2	2.818×10^{-8}	2.381×10^{-9}
p_3	1.184×10^{-11}	1.398×10^{-12}

Table 5.1: List of calibration fit parameters with its errors.

In figure 5.3 the resulting 2D H-band spectrum is shown based on the total integration time of 10.8 s. The edges of the spectrum are cut away due to non-linear flat fielding effects at the filter extremes. At the red (long-wavelength) end, the Q and R branches from the 6-4 transition can be seen. The other three resolved transitions belong to the 3-1, 4-2 and 5-3 transitions. The signal to noise ratio is up to 280 for the Q-branch lines and around 200 for the P-branch lines. Longer exposure times would increase these ratios further. The total pixel intensity scale on the y-axis is proportional to the photon count rate by a constant factor of 2.5 at these low intensities[36].

5.2.3 Line selection

Not all the lines from the OH bands can be fit with a rotational temperature that is equilibrated with the ambient atmosphere in the MLT. As mentioned, Pendelton et al.[39] and Cosby and Slanger[28] have shown that transitions arising from rotational levels greater than four do not thermalize to the ambient temperature. Thus, any lines arising from these levels are eliminated from the data to be fit. Additionally, lines near the long and short wavelength edges of the detector lie in the cutoff region of the optical filter and cannot be accurately flat fielded. Thus, lines within 50 pixels (approximately 150 nm) of the detector edge are not used in the fitting. Finally, lines that are absorbed by water vapour in the lower atmosphere would vary as the water vapour content of the atmosphere varied. Thus lines identified as lying within 30 nm of water vapour absorption features[40] are not used. Two other reasons will be discussed here as main reasons for line selection.

The most simple reason would be an absorption or scattering of the line from the atmosphere between the OH layer and the measuring array. That is for example the case for the whole P-branch of the 6-4 transition. The lines are absorbed by the filter for the H band.

The other reason is an overlap between the lines of one transition with the lines of a neighbouring transition. This is more important for the transitions with small v'. Whether lines from neighbouring transitions perturb the observed lines is not only dependent on the inherent line strength and position in the spectrum, but also from the concentration of OH in this vibrational state and the noise background of the measured spectrum. However, a perturbation from neighbouring transition that is smaller than the noise level of the current transition is negligible.

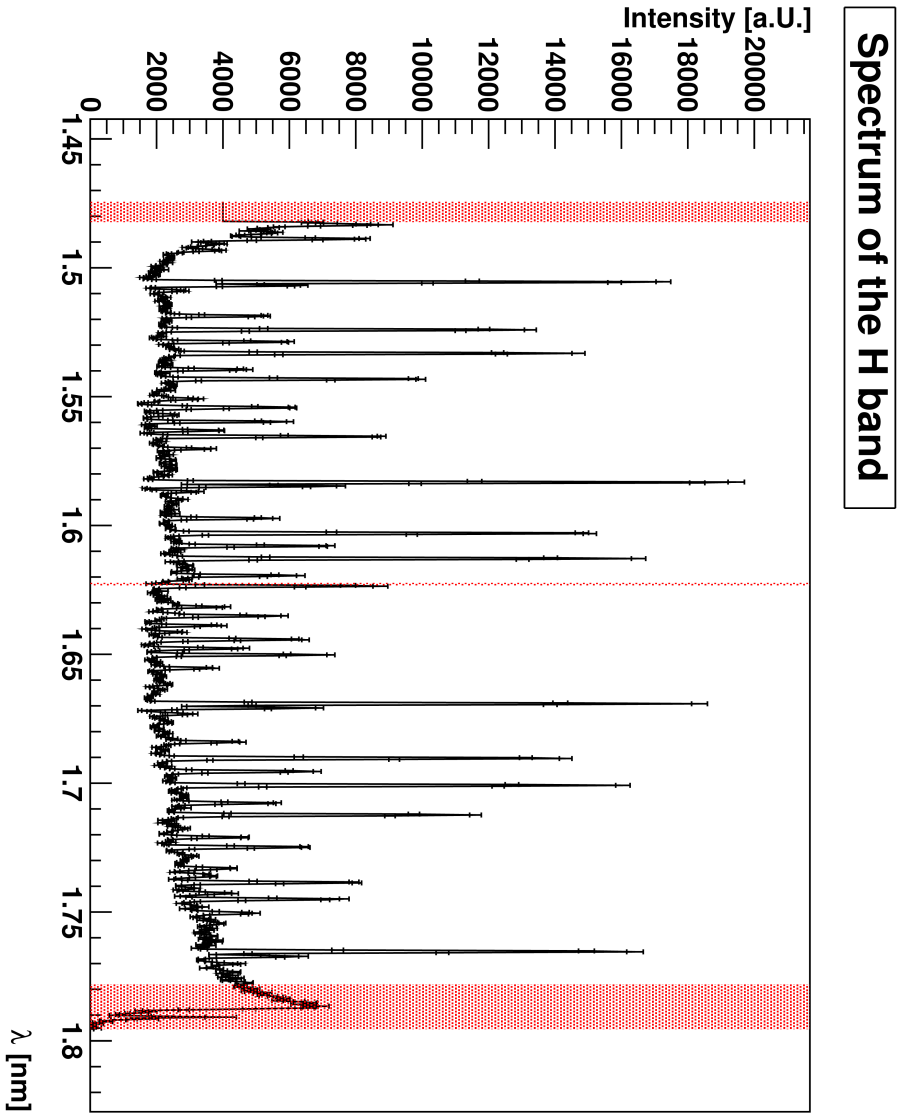

Figure 5.3: Spectrum of the whole H band of this measurement. The x axis was calibrated to wavelengths in μm. From left to right, one can see the transitions 3-1, 4-2, 5-3 and the R and Q-branch of the 6-4 transition. This spectrum is directly coming from figure 5.1. Areas were array edge efects perturbe the spectrum are shaded red, and ignored in the subsequent analysis. The 30 pixels at the left are the ones that are not in the mapping area of the straightening and therefore just set to the value of 4,000.

To test where an overlap occurs, the spectrum is modelled. For this, the temperatures of the transitions have to be known approximately, as this will change the rotational distribution (see figure 2.6). Higher temperatures will lead to more intense transitions from the higher rotational levels that may overlap with adjacent bands.

To provide an estimate of temperature in order to identify overlapping transitions, a rough line selection was done by hand. These line selection is based on the lines that are within the filter range of the NOTCam. To these lines, a temperature was fitted, called T_{approx}. In all cases later on, T_{approx} is only a few degrees off of the real temperature. This is done for the transition in question, as well as for the neighbouring ones. Effects from second neighbours were neglected.

Next, model spectra are created with the help of the HITRAN data. The models are the same vibrational transitions, population N_o and the rotational temperature as the experimental transitions. They are left unperturbed[2] but are broadened with the same width as the measured lines. These unperturbed models (synthetic spectra) are then all three added up (in this example for the transitions 4-2, 5-3 and 6-4). Then the ratio of the intensity of the synthetic spectra for the transition in question (here 5-3) to the sum of all three is calculated for each wavelength. All the lines are shown in figure 5.4.

If this ratio now drops lower than 0.99, the corresponding wavelength region will be neglected afterwards. The 0.99 boundary is shown as a solid black line in figure 5.4. One can see, that at the verges of the 5-3 spectrum, the neighbouring transition lines become important and lines from the 5-3 transition are ignored. This is for example the case here for the $R_2(2)$ and the $R_1(2)$ lines.

As mentioned before, if for a given pixel the contribution from the neighbouring transitions is smaller than the error for this pixel, an overlap is ignored.

5.2.4 Noise measurement

An approximate noise content of the data presented in this thesis, is shown in figure 5.5. The signal to noise level, presented in figure 5.5 is the signal to noise ratio[3] of the highest line in the 9-7 transition. This highest line is the $Q(1)$ line. The data were plotted with this signal to noise level against the integration time of this measurement.

There are various sources of noise for the NOTCam. The read out noise is known to be 8 to 9 electrons (approximately 3.5 counts) for one readout[37]. Since the readouts are interpolated as discussed in section 4.1, the readout noise goes with $\sqrt{N}$, where N is the number of readouts.

The signal noise is a poisson error on the number of photons measured. It goes with the squareroot of the integration time $\sqrt{t}$. The same is true for the noise of the dark current. It is found that the signal noise is the dominating here.

Therefore, a simple square root function was fitted to the data. The relatively low χ^2 per degree of freedom value of the fit shows that the constant parts in the

[2] Unperturbed means here that no noise was added to the synthetic spectrum.

[3] As mentioned in section 5.1, the noise value for a line is the standard deviation of all pixels from the array, which belong to this line.

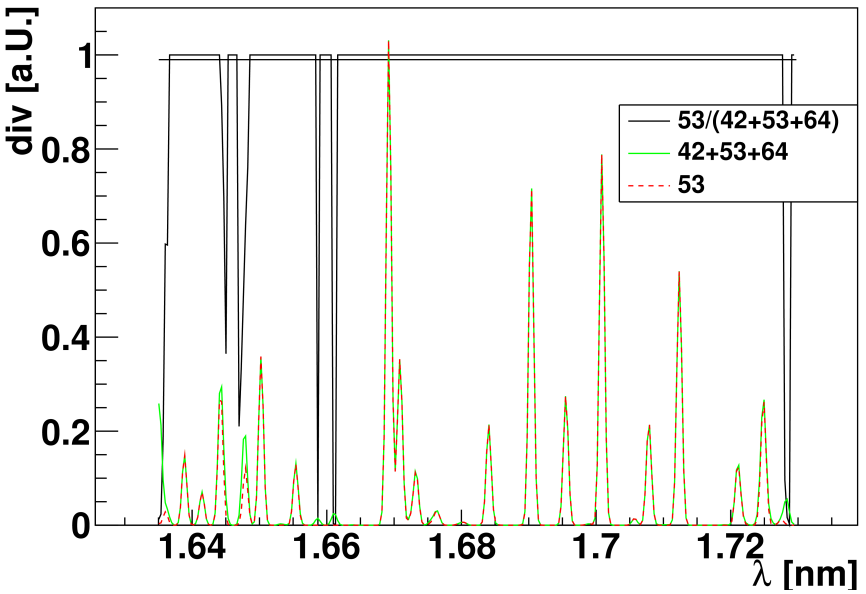

Figure 5.4: Check of the overlap for the 5-3 transition. In red, the spectrum of the 5-3 transition is shown, in green, the sum of this and its neighbouring transitions. The y axis for these spectra would be intensity in arbitrary units. In black, the ratio of both is shown. If this ratio drops under 0.99 (shown as a horizontal line at the top) for a given wavelength region, this region will be ignored because of the perturbation of the neighbouring transitions.

noise dependency are low in comparison to the pure statistical noise.

However, this is only an approximate measurement, since not many data points were available. It is more to be seen as a rough idea than a precise measurement.

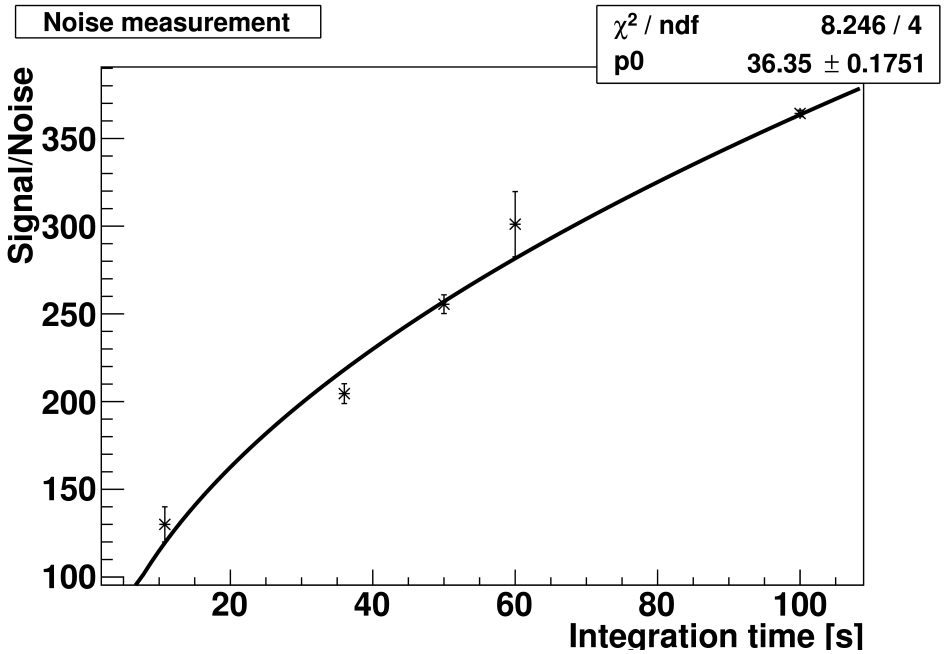

Figure 5.5: Approximate noise measurement of the NOTCam. The data used later in this thesis was plotted for the 9-7 transition in the K band with integrations time in seconds versus the signal to noise ratio of the highest peak ($Q(1)$). A simple square root function $f(t) = p_0\sqrt{t}$ was fitted to the data, since the signal noise is dominating. The fit result and the χ^2 value per NDF (number of degrees of freedom) is stated in the box in the upper right corner.

5.2.5 Filtering

As can be seen in figure 5.3, the background is not completely flat but has, in addition to the high frequency noise, low frequency variations. Here, low frequency refers to variations that span a range of wavelengths greater than the OH line widths. Since these variations in the background will influence the relative intensities of the individual rotational lines, they can have large impacts on the eventual fitted OH rotational temperature, as the temperature is strongly dependent on the relative heights of the lines. For this reason a high pass Butterworth filter with a pass frequency of $1/3\,\mathrm{nm}^{-1}$ and a stop frequency of $1/6\,\mathrm{nm}^{-1}$ was employed on the extracted 2D spectra to remove the low frequency variability with minimal impact on the (high frequency) OH rotational lines. A pixel translates approximately to 0.3 nm and the width of a line is approximately 0.31 nm.

After filtering, the spectrum was normalized such that the absolute area under the spectrum is equal to one. As a filtered spectrum shows the individual rotational lines as peaks in both the positive and the negative direction (see figure 5.6, where the filtered spectrum for the 5-3 transition is shown), the normal integral (i.e. the sum over all data points) is small, whereas the absolute integral (i.e. the sum over the absolute values of all data points) yields a more precise normalisation.

The normalization constant is directly proportional to the population of the rotational level v', N_o from equation 2.9. This value will be fitted as well later in section 8.1.

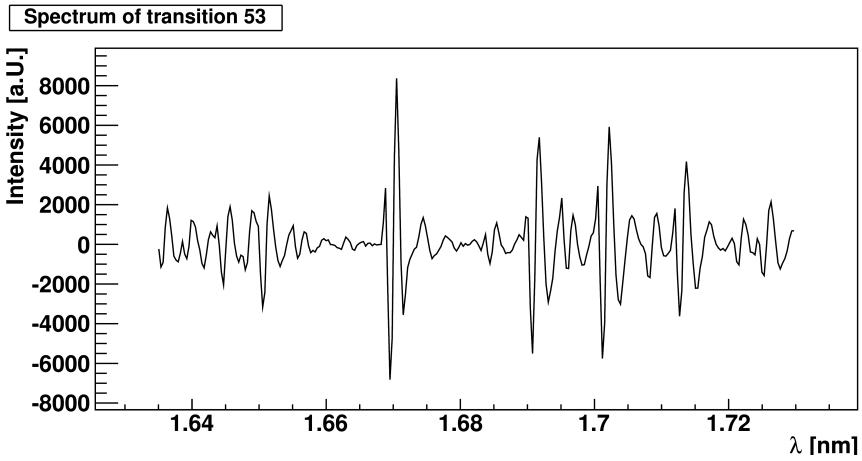

Figure 5.6: Filtered spectrum of the 5-3 transition. The constant offset and the low frequency variability parts are no longer visible.

The filtered, normalized spectrum is now only dependent on the rotational temperature T_{rot}, the background level being equal to zero.

If a wavelength region is neglected in the inside of the spectrum due to an overlap from other transitions a pause in the signal for the filtering will arise. This neglection happens here for example between the Q-branch and the R-branch. The

pause is created since the values at the overlap are dropped. This is no problem to the filtering- and fitting routines later. To prove this, a region without lines was removed from a spectrum. Then, the temperature was fitted to this spectrum and the original one with all data points. The result of the temperature was unchanged. Only the error on this value increased a little for the spectrum with a pause. The larger error occurses because less data points are available for the RMS calculation that leads to the error calculation.

5.2.6 Temperature fitting

The central idea presented in this thesis is the creation of a model spectrum without added noise for a given rotational temperature. This test data uses the same, unperturbed lines as the data. This model spectrum is filtered and normalized as the data. A χ^2 minimisation using the rotational temperature as the variable parameter can now be performed between the model and the data to find the temperature that best fits the data.

This procedure may be contrasted with that of Noll et al. [1], where the intensities of the individual rotational lines in their high resolution spectra could be fitted directly with the Boltzmann relation (equation 2.9) to yield a rotational temperature. If this procedure was implemented here, it would mean that only resolved peaks could be used. Given the broader line shapes of the NOTCam, this would severely limit the number of lines that could be fit. For example, the most intense Q-branches with high signal to noise ratio could not be used since they are unresolved. Thus the spectral model approach was adopted.

Figure 5.7 shows the spectrum from figure 5.6 again, this time with the fitted model spectrum shown as the red line. The model fits the data very well. The fitted temperature is $188.0 \pm 0.56\,\mathrm{K}$. The error is $0.3\,\%$ of the value. The residual spectrum can be found in figure 5.8. It varies around zero, mostly within the statistical noise background. A small variation can be seen at some of the peaks, best at the $Q(1)$ line at approximatly $1.67\,\mu$m and the $P_1(2)$ line at approximatly $1.702\,\mu$m. The effect is symmetrical around the peak centre and small. It indicates a small difference between the real line shape and the modelled line shape. This mismatch is small enough to not change the results.

This residual in figure 5.8 demonstrates that the model used is robust and that fitting to the high pass filtered data works as it should, and that the fit to the data converges to a temperature with a small error when spectra are extracted from an observation based on *just 10*s *of total integration time*. The implications of this for future potential atmospheric physics applications are discussed in chapter 8.

5.3 Implementation

For this master thesis, an evaluation framework was created as a user-friendly tool for future reduction of spectroscopic data by the NOTCam. With the help of this program framework, all the plots that are not specifically copied from other sources, were created. The framework employs different programs and environments.

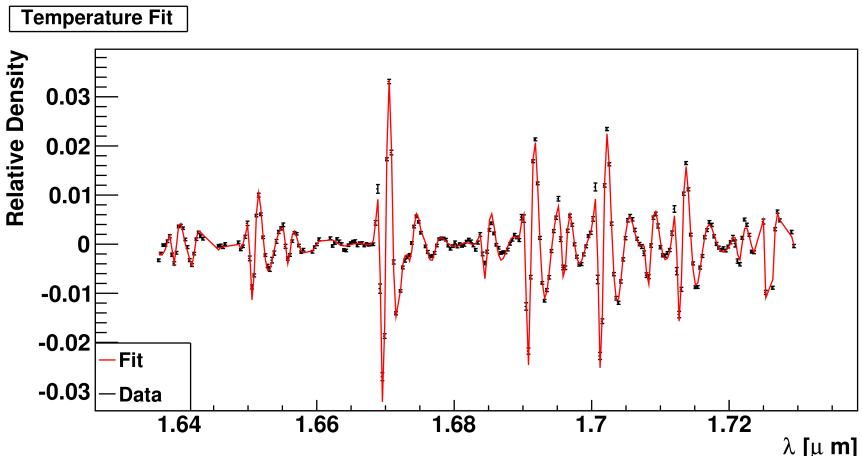

Figure 5.7: Spectrum from figure 5.6 (black) fitted by employing a χ^2 minimization with a filtered model spectrum (red). The resulting temperature is $188.0 \pm 0.56\,\mathrm{K}$. This error margin is quite small for a simple 10.8 s integration.

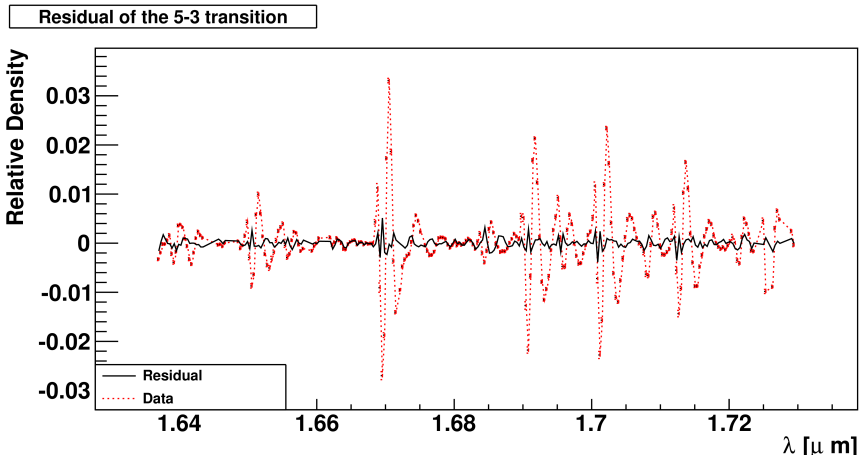

Figure 5.8: Residual plot of the fit from figure 5.7. The black continuous line is the former spectrum minus the fitted model spectrum. The red, dashed line represents the filtered data before fitting. One can see that the model and real spectrum fit together with respect to the noise level.

The first steps of this chapter are done in IRAF[38], a standard tool for astronomical data reduction. Beginning with the removal of the star's spectrum, the code is self-written. For this purpose, a C++ class *Spec* was written. The version C++11 was employed. An object of this class holds all information of a single spectrum. This can either be a spectrum from a NOTCam picture or an artificial

model spectrum. The class does the further reduction steps automatically during construction of the object. The evaluation steps (so the fitting and the figure creation) can be done separately.

The fitting routine and most of the plotting is done by the help of the ROOT library[41]. A full documentation for this library can be found at [42]. The fitting routine itself internally uses the open source fitting routines from Gnu Scientific Library (GSL)[43]. A BRENT algorithm[44] was used for minimisation of the χ^2 function. This algorithm is a combination from a parabolic interpolation and a golden section algorithm. For further information on the algorithm, see [44] or the GSL documentation in [45]. The error on the temperature fit is calculated from the RMS values of the residuals. The errors are tested and verified in section 7.1.

The plots for three dimensional problems, so the plot of the array pictures, were done by the help of GNUPlot[46]. The contour plots from chapter 8 were generated by the framework but plotted by Matlab[47].

The framework in C++ is very easy to use, clear and easy to understand. Thereby, more complex usage (as for example demonstrated in section 7.1) of the framework is easy as well. As an example, the most important commands are given in a functional example below:

```
#include <../sys/typicalIncludes.h>//Includes all important parts for
    the most cases.
int main(){
  Spec *s = new Spec("File.fits",53);
    //Creates a new Spec object of the file "File.fits" for the 5-3
    transition
  s->printImage("Image");
    //Prints the array
  s->printCal();
    //Print the calibration fits as figure 5.2
  s->printOverlap();
    //Print the overlap as in figure 5.4
  s->printSpectrum(true);
    //Prints the spectrum as in figure 6.2. "true" means that the
    errorbars are drawn
  s->filter();
    //Filters the spectrum
  s->printSpectrum("filtered",false);
    //Prints the spectrum as in figure 5.6
  s->normalize();
    //Normalizes the spectrum
  s->printSpectrum("normed",false);
    //Prints the spectrum after normalization
  s->fitTemp();
    //Fits the rotational temperature
  cout << s->getTrot() << " +/- " << s->getSigmaTrot() << endl;
    //Drops the fitted temperature with error to the shell
  s->printFit("Temp");
    //Prints the fitted spectrum as in figure 5.7 and its residual plot
     as in figure 5.8
  s->fitInt();
    //Fits the intensity
  cout << s->getNo() << " +/- " << s->getSigmaNo() << endl;
    //Drops the fitted intensity with error to the shell
```

```
31    s->printFit("Int");
        //Prints the fitted spectrum as in figure 8.3 and its residual plot
33  }
```

The framework is constructed open, such that it can be improved and expanded at any time, as well as all data from a *Spec* object can be accessed from within the program with the given getter functions.

Chapter 6

Results

6.1 Data used

For this thesis, six observations were available from routine observations archived at the NOT. They are listed in table 6.1. The data were taken on two different days. The first observation was already presented in the chapters 4 and 5. The other five observations were all taken in the same night. Note, that for the first three, taken shortly after midnight, only the K band was available. During this night, no darks were taken for these observations specifically. Therefore, darks taken for another observation were used. This could cause minor perturbation, but none could be found specifically.

name	date	time UT	integration time [s]	air mass	bands
NCwb19	19.02.13	5:48-5:54	10.8	1.52	H,J,K
NCvi06 1	06.09.12	0:06-0:12	60	1.23	K
NCvi06 2	06.09.12	0:14-0:18	36	1.26	K
NCvi06 3	06.09.12	0:31-0:36	60	1.24	K
NCvi06 4	06.09.12	4:34-5:06	100	1.19	H,J,K
NCvi06 5	06.09.12	5:23-5:39	50	1.10	H,J,K

Table 6.1: List of the data used in this thesis with the date (of the evening of the observing night), when the data were taken, the integration time and the bands taken for this observation.

The observations from the 06.09.2012 cover a good part of a night. Variations through the night can be evaluated with this observation.

The integration time stated in table 6.1 is the integration time for one image. Between each two images, the readout of the data needs approximatly 10 s of down-time. Each observation contains 4 of these images for the ABBA sheme for each filter. Therefore, the observation NCwb19, NCvi06 4 and 5 contain 12 images. The observations NCvi06 1, 2 and 3 contain 4 images. Additionally, darks and lamp images are done during the night. These images are mostly taken at the end of the

night. If the star to be observed was different for two observations, the telescope had to be moved as well, which can take up to a few minutes.

6.2 Spectra

In table 6.2, the detectable bands are listed together with the well resolved branches cross referenced to the spectra plotted in Figure 6.2 and 6.3.

Transition	Band	Branches fitable	Plot
3-1	H	Q P	6.2
4-2	H	Q P	6.2
5-3	H	R Q P	6.2
6-4	H	R Q	6.2
7-4	J	Q P	6.3
8-5	J	R Q (P)	6.3
8-6	K	P	6.3
9-7	K	R Q P	6.3

Table 6.2: The branches observed in the different transitions and the reference number to the plots of the bands for the observation NCwb19.

Figure 6.1, shows the full spectrum of the H, J and K-bands. The horizontal lines represent the parts of the spectra, shown in figure 6.2 and 6.3. As in figure 5.3, the unusable parts are shown in red. The J band is less intense than the other two bands. This is because the transitions of the J-band have a $\Delta v = 3$ instead of $\Delta v = 2$ as the transitions in the other two bands. Also, the spectra are not yet absolutely calibrated for intensity. This calibration can be done with the observed spectra of standard stars. The intensity calibration is left for further research.

Figures 6.2 and 6.3 show an overview of all the measured OH vibrational transitions recorded in the H, J and K band spectra taken towards the same standard star, extracted in the manner outlined in chapter 5. The data is from the observation NCwb19 from the 19.02.13. All spectra were taken with the same 10.8 s (3×3.6 s) integration time. For the majority of vibrational transitions, the signal is very much larger than the noise, providing good temperature fit conditions. In the above case, for the spectrum of the 5-3 vibrational band of OH, the P and Q branches lie well within the detectable wavelength regions. In the R-branch, the lines $R_2(1)$, $R_1(1)$, $R_2(3)$, and $R_1(3)$ are visible, while the lines $R_2(2)$ and $R_1(2)$ are overlapped by neighbouring transition lines. The fitting routine employed used the first four rotational lines of the P branch of the transition as the higher lines overlap with the R branches of the next vibrational band. This is also the case for the 7-4 and 4-2 transitions.

The 8-5 vibrational band, seen in figure 6.3, lies directly on the edge of two segments of the NOTCam detector array. This edge is shown in red in figure 6.1. It lies directly on the $P_1(3)$ line. This leads to an artefact in the final extracted spectrum of a similar magnitude to the rotational lines and can therefore not be

filtered away without filtering away the data as well. Fortunately, for this band the R branch is clearly resolved, as the P branch of the 7-4 transition lies far enough away. However, since the J band comes from the transition with $\Delta v = 3$, the lines are not as intense as in the ones of other bands. Therefore, the temperature measurement will be less precise. Additionally the R-branch is of lower intensity than the P branch, hence the line's signal to noise is lower and the resulting fitted temperature less precise. However, it should be noted that all data presented here are the result of a single 10 s integration time measurement. Longer integration times (or co-adding multiple images) can be used to enhance the data quality. Since the 8-5 transition is not optimal, the 8-6 transition becomes important. Here, the NOTCam filter removed the Q-branch, but most of the P branch is well resolved and can be used for fitting. However, with not many lines left and the intense lines not available, the fit is going to be a little more unstable and will yield larger errors.

The P branch of the 6-4 transition does not fall within the wavelength region of the NOTCam H-band-filter, but again, the R-branch of this band is well resolved and separated from the neighbouring (5-3 transition) P-branch and can be used for temperature fitting. Finally the 9-7 transition representing the highest vibrational state formed by the reaction 2.1, has well resolved Q, R and P-branches which makes precise fitting possible.

The bands do not have equal quality. The J band for example is less intense than the others. Therefore, the J band will have a lower signal to noise ratio.

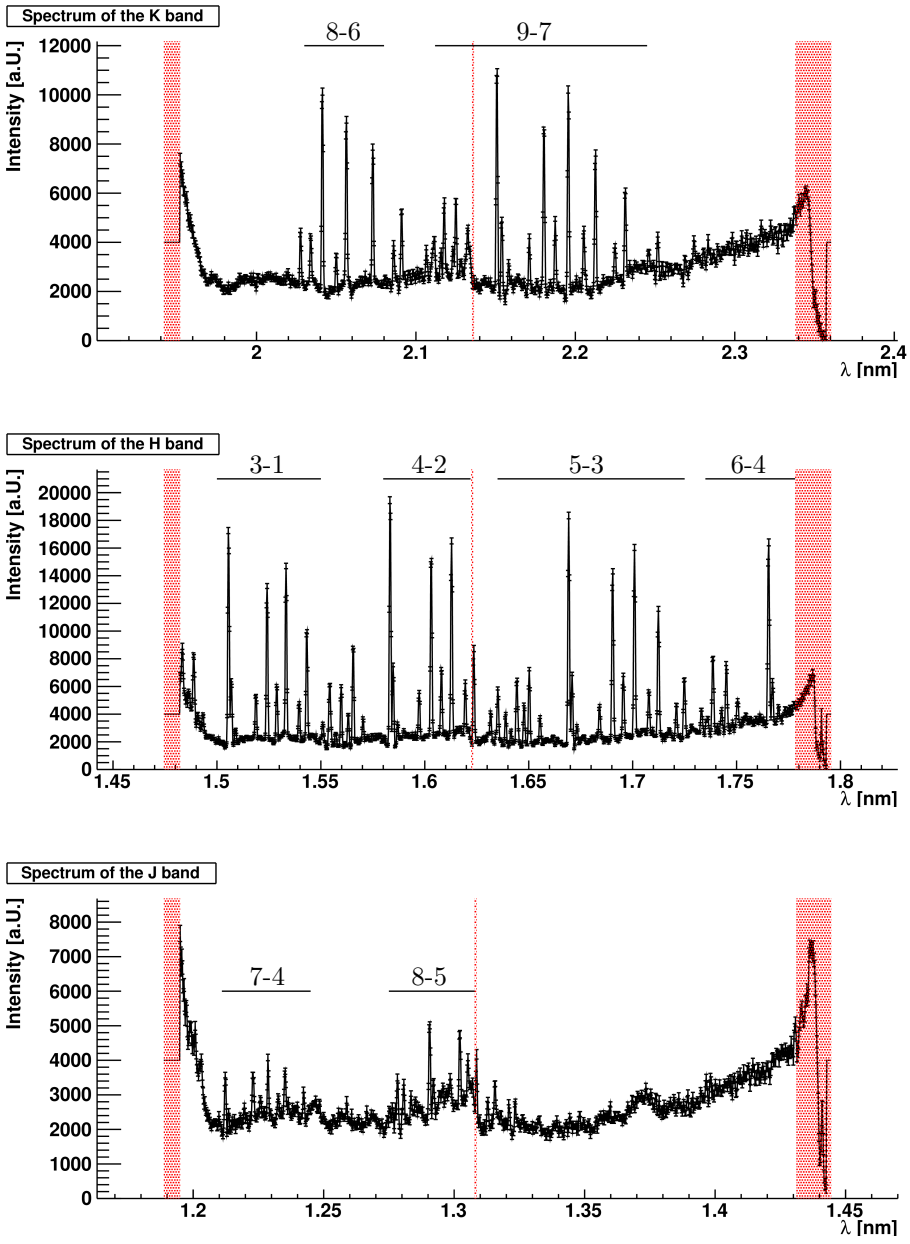

Figure 6.1: Overview over the H, J and K band spectra from the observation NCwb19. The transitions in the band are labelled. The horizontal line for each transition indicates the part of the spectrum shown in detail in the figures 6.2 and 6.3. The unusable parts of the spectrum are showed in red as in figure 5.3

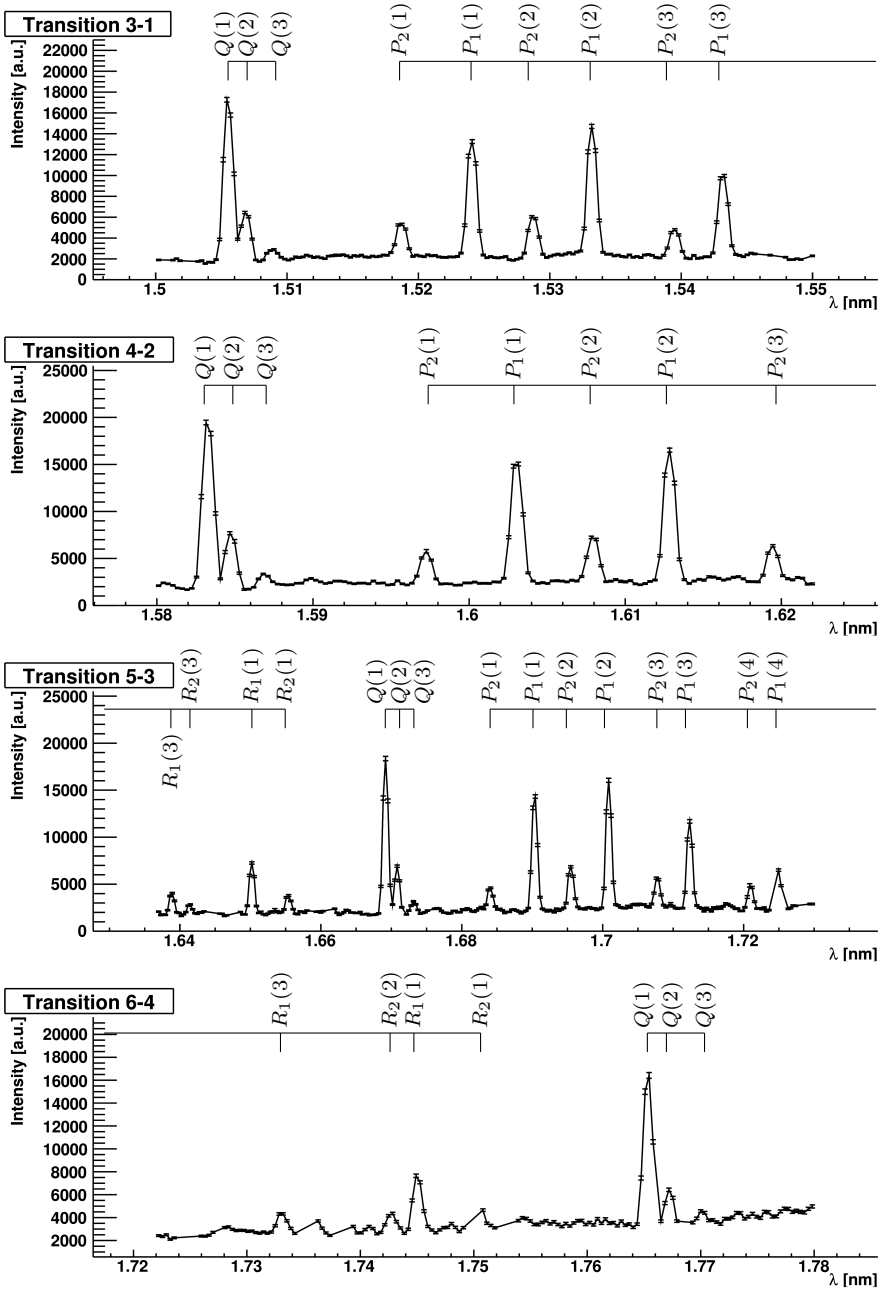

Figure 6.2: Spectra from the H band from table 6.2

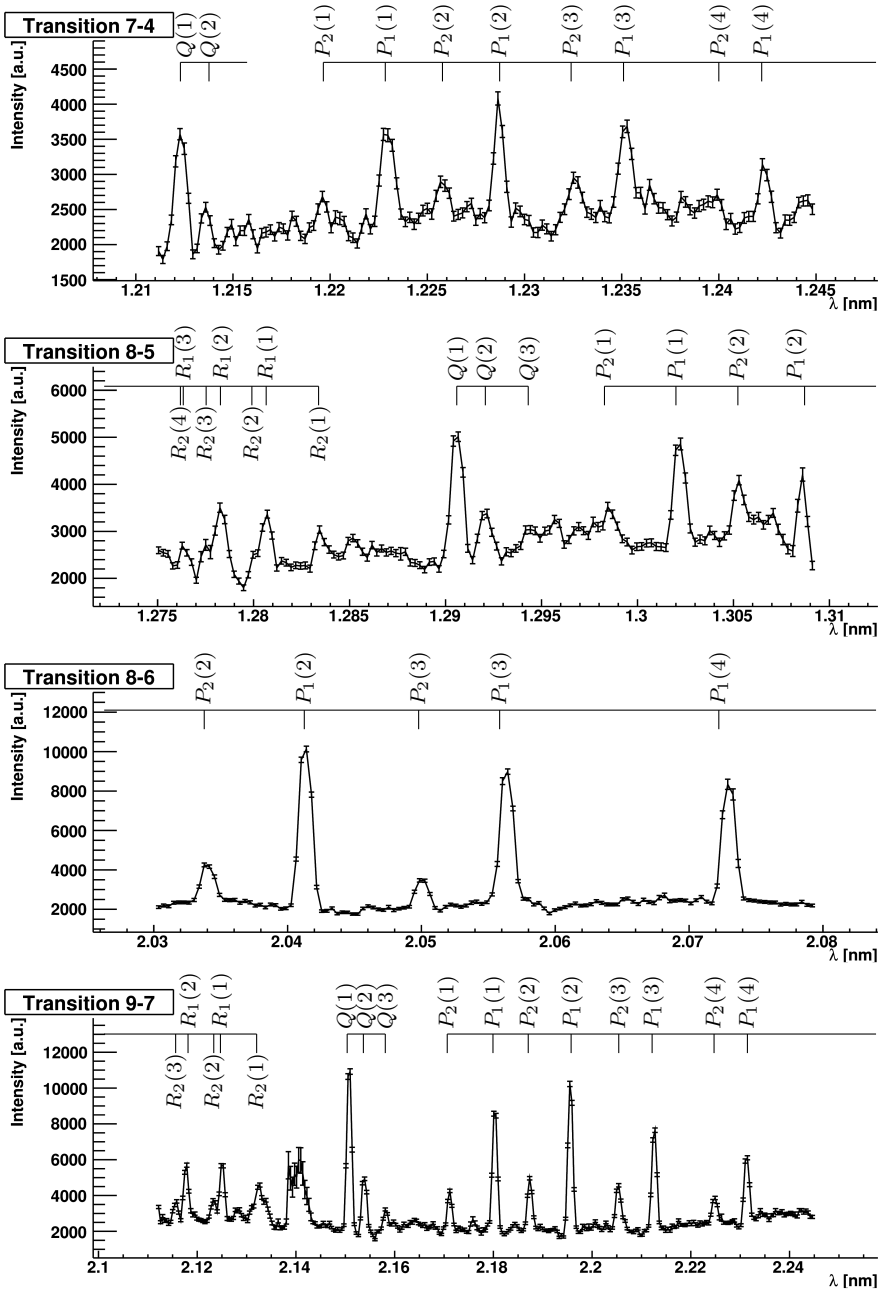

Figure 6.3: Spectra from the J and K band from table 6.2

6.3 Temperature fits

For all these spectra, the rotational temperature was fitted. The results for all the fits for this observation can be found in table 6.3.

Transition	T_{rot} in [K]	$\sigma_{T_{\mathrm{rot}}}$ in [K]
3-1	190.0	0.78
4-2	189.6	0.98
5-3	188.0	0.56
6-4	186.9	1.59
7-4	228.5	4.90
8-5	190.3	2.71
8-6	192.8	1.75
9-7	182.9	0.70

Table 6.3: The fitted results for the rotational temperature for the observation NCwb19. The usable branches can be found in table 6.2. The spectra are shown in figures 6.2 and 6.3.

6.3.1 Temperature - altitude dependency

With the rotational temperature for each transition fitted and the altitude difference between transitions known from [48] to be half a kilometre for neighbouring transitions, the altitude dependency of the temperature can be found. In figure 6.4, the eight temperatures from table 6.3 are plotted against their relative height to each other.

As discussed above, the transitions in the J band have very low intensity. The 8-6 transition as well is perturbed, as the Q-branch and the beginning of the P-branch do not lie inside the filter area. In the figure 6.4, one can observe that exactly these three transitions (plotted in red) are very different from the overall trend. As discussed later in section 7.2, Noll et al.[4], also observed that the transitions from $v' = 8$ yield a too high rotational temperature. The 7-4 transition yields a very high rotational temperature with a large error bar.

For the other five points, a downward straight line was fitted ($T(z) = p_0 + p_1 z$). The χ^2 value per NDF is remarkably small. However, it is to consider that there are only 3 degrees of freedom. The coefficient of linear correlation is with -0.994 very close to -1. This coefficient shows, that the data have a linear relationship. Since the z-scale is only relative, the parameter p_0 has no deeper meaning. The slope p_1 on the other hand is of greater meaning and represents the measured T gradient $\mathrm{d}T/\mathrm{d}z$ at the time of observation. The analysis of this temperature gradient is presented in section 7.3.

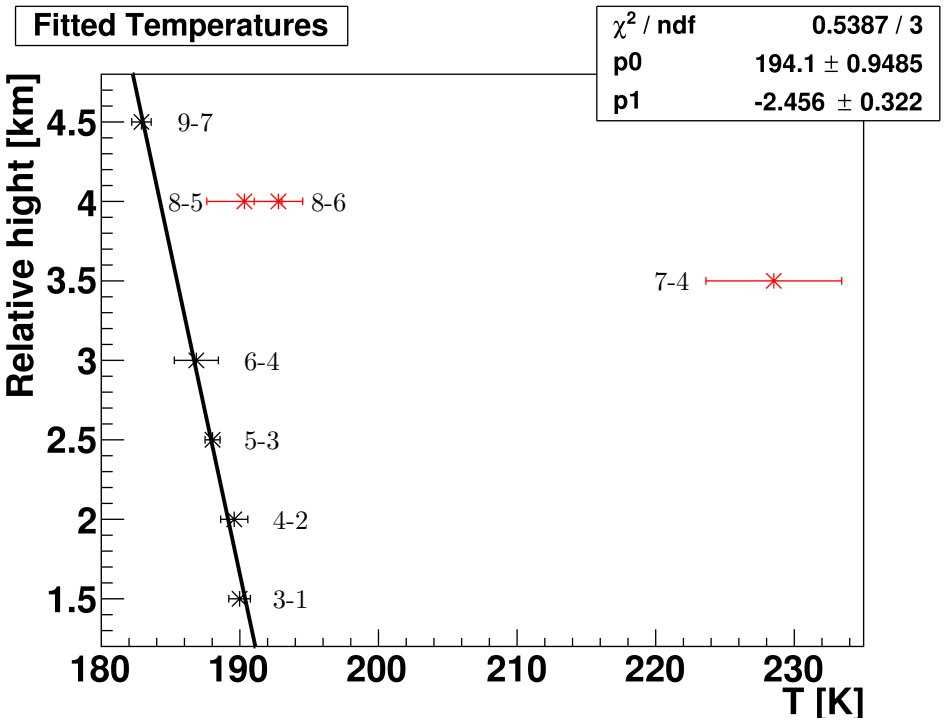

Figure 6.4: The fitted rotational temperature for the observation NCwb19 from table 6.3. The transitions 7-4, 8-5 and 8-6, plotted in red, are clearly outsiders. The rest are fitted by a descending straight line. Since the altitude axis is in relative numbers, the value p_0 is arbitrary and only depends on the chosen height of the lowest transition (here 1.5 km). Each point is labelled with its transition.

6.3.2 Temperature - time dependency

The same evaluation from chapter 5 was done for the observations NCvi06. These observations offer a wide range of times during one night (see also table 6.1). When available, all four measurements from the ABBA scheme were evaluated and the results averaged. In table 6.4, the data frames available are listed. The last measurement only has two working data frames, the rest all have at least three.

Note that this is only done for the observations NCvi06. Therefore, all results presented until now, are only the results of one image with 10.8 s integration time.

In figure 6.5, the fitted temperatures for the 8-6 transition and the 9-7 transition were plotted over the times of the observations. Only these two transitions were available for all times. Both temperature profiles follow each other and show the same development. This behaviour was expected, as the bands are only about half a kilometre vertically away from each other in the atmosphere[48]. The statistical

name	A	B	B	A
NCvi06 1	x	x	x	
NCvi06 2	x	x	x	x
NCvi06 3	x	x	x	x
NCvi06 4		x	x	x
NCvi06 5			x	x

Table 6.4: List over the available data frames from the ABBA scheme. An x means, the data frame was available.

error on the temperature is smaller than the variations between the temperature results for the different observations. This makes the temperature profile likely not to be an artefact of fitting or noise.

From figure 6.4, it is known that the temperature of the 8-6 transition is around 8.5 K away from the expected value from the temperature gradient. The measured time development of the 8-6 transition was therefore shifted down by 8.5 K. It brings the temperature profiles very near to each other. It seems like that the temperature gradient reversed in this part of the atmosphere in the end of the night.

name	time UT	$^{\mathrm{d}T}/_{\mathrm{d}z}$ in $^{\mathrm{K}}/_{\mathrm{km}}$
NCvi06 1	0:06-0:12	−8.51
NCvi06 2	0:14-0:18	−7.84
NCvi06 3	0:31-0:36	−5.89
NCvi06 4	4:34-5:06	−3.51
NCvi06 5	5:23-5:39	−2.29

Table 6.5: Temperature gradient from different times in the night of the 06.09.12. For the first three observations, only the K-band was available and the gradient was calculated from the 8-6 and the 9-7 transition. Since the 8-6 transition yields a too high temperature for all observations observed, the gradient becomes very small for these.

The gradient was calculated similar to figure 6.4 for the observations NCvi06 4 and 5. Since the first three of the observations for that night only offer the K-band, the $^{\mathrm{d}T}/_{\mathrm{d}z}$ for these times was calculated using only the 8-6 and the 9-7 transitions. Note, that the 8-6 transition is from figure 6.4 likely to be too high. This yields a too small $^{\mathrm{d}T}/_{\mathrm{d}z}$.

The results for the temperature gradient for all five times can be found in table 6.5, together with the times of observation from table 6.1.

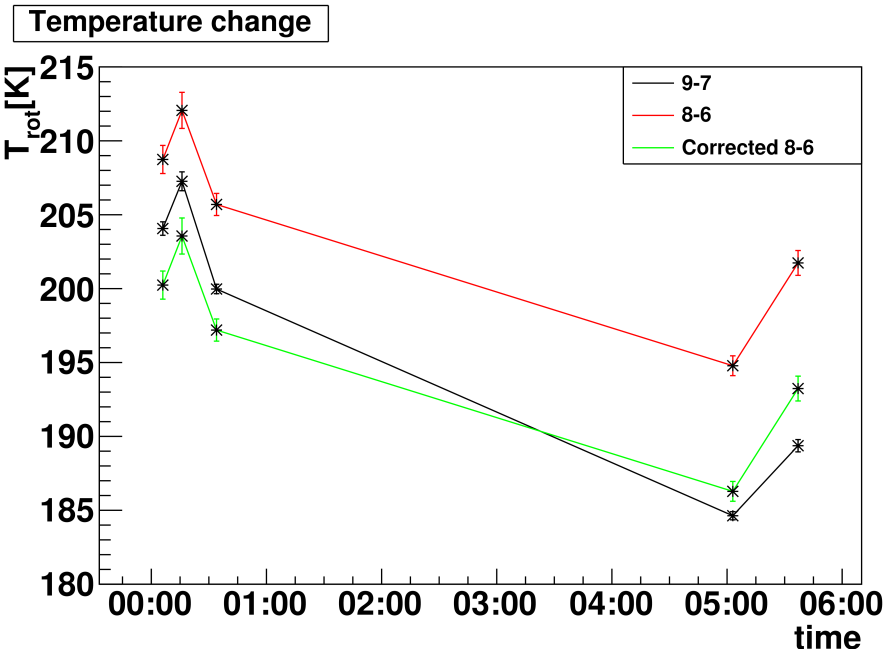

Figure 6.5: Variation of the rotational temperature over time. The observations NCvi06 were employed. Since the K-band was available for all times, only the 9-7 and 8-6 transitions are shown. The green graph is the 8-6 transition shifted downwards by 8.5 K, since this is the known deviation of the 8-6 transition to the expected temperature from the temperature gradient from figure 6.4.

Chapter 7

Data validation

The results presented above seem to present a coherent picture. In this section, I demonstrate by comparison with synthetic test data created with the HITRAN[2] data, CIRA86 [18] data and previous work by Noll et al.[4] that the analysis procedure is robust, reliable and consistent with previous work.

7.1 Verification with synthetic test data

The first check has to be whether the fitting routine of the framework is working for the rotational temperature T_{rot}. The broad aim behind the tests outlined in this section is to create a spectrum of synthetic test data with given parameter T_{rot} [1] and signal to noise ratio, and then fit it with a spectrum, as used in the fitting routines used for this thesis. The parameters of the synthetic spectrum can then be related to the ones of the synthetic spectra. For this section, the 5-3 transition is used to demonstrate the principle, however all results are repeatable with different transitions.

An example for this procedure can be found in figure 7.1. There, a test data with T_{rot} =200 K were fitted again. The test data were perturbed with white gaussian noise.

First, T_{rot} will be verified. For this, the test data parameter N_o is not important, as the spectrum will be normalized either way. The signal to noise ratio was varied in a range of values that were observed for the NOTCam. Already in figure 5.5 these typical values were shown. In the example below, the signal to noise ratio was set to be 200. The result does not change, when varying this ratio between 100 and 400.

The test data are perturbed with pure white Gaussian noise with a width of the inverse signal to noise ratio times the height of the highest peak. This simulates the noise on a real spectrum. Although a real spectrum has the additional perturbations, described in section 4.2, these are taken to be small and are not modelled.

[1] and an arbitrary N_o. This parameter is not important after normalization.

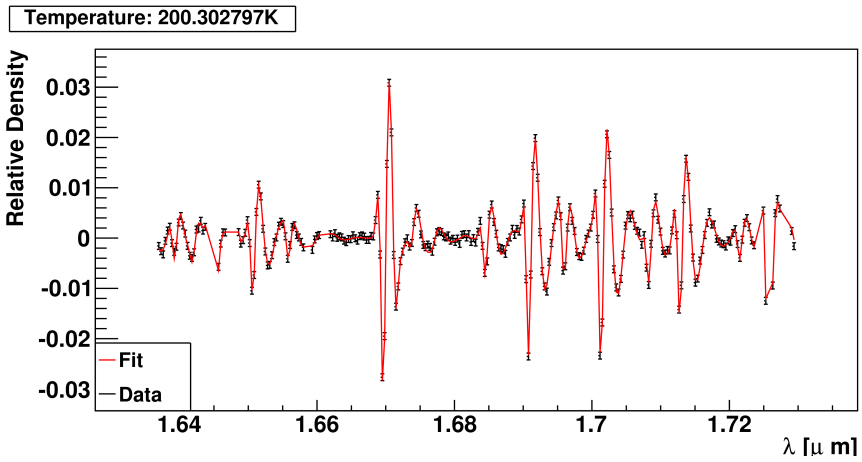

Figure 7.1: Example of the fit to synthetic test data. The test data were created for the 5-3 transition and T_{rot} =200 K. Then, they were fitted again. The test data are shown in black, while the fit is shown in red. The result for the temperature is 200.30 K $\pm$ 0.63 K

The same fitting routine as in previous chapters, including the same line selections were employed.

From the CIRA86 model[18] only temperatures well in the range between 150 K and 300 K are expected. In figure 7.2, T_{rot} of the synthetic test data was varied between 50 K and 400 K. The temperature range was chosen bigger than expected from the CIRA86 model to account for strong deviations from the model results. The fitted temperature is plotted in figure 7.2 for the different synthetic test data temperatures.

It is clear that the fit yields the correct result between 150 K and 400 K. For the lower temperatures, the higher R and P-branch lines are very small. If these lines become approximatly ground level (starting below 150 K), the noise is relatively large. If the noise makes the line higher than they are, the fit can assume a too high temperature. But if the noise makes the lines smaller, the line's value would be smaller than ground level. The fit cannot acount for that, since only positive lines are in the synthetic spectra used for fitting. In this case, the noisy line can only be ignored by the fit and the result for the temperature is not changed in a specific direction. Therefore, for these temperatures below 150 K the fit is likely to yield too high temperatures.

This result verifies the temperature result of the fit for the important temperature range between 150 K and 300 K. This temperature range will be used in the following.

In order to test the error estimate from the fitting, 60 model spectra were generated at a given rotational temperature T_{rot} but with different realizations of white noise. Because of this different background noise, the fitting result is expected to differ a little. The statistical standard deviation of the results on T_{rot} , σ_{stat},

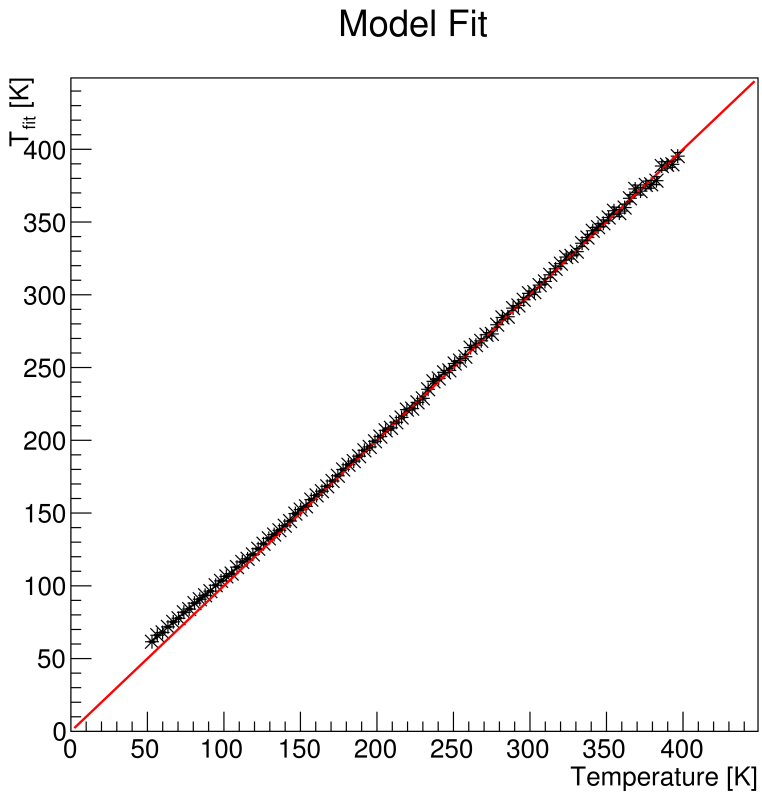

Figure 7.2: Verification of the fitted temperature. T_{rot} of the synthetic test data was altered between 50 K and 400 K. The fitted temperature is shown for different temperatures of the test data. In red, the line $T = T_{\mathrm{fit}}$ is shown. Only for temperatures smaller than 150 K, the fitted temperature deviates from this line. This figure shows that the fit yields consistent results for temperatures between 150 K and 400 K.

can then be calculated, and compared to the estimate of uncertainty on each single fit σ_{fit}. This test is performed over a range of simulated rotational temperatures from 150 K to 300 K.

For each value of T_{rot} , the ratio $\sigma_{\mathrm{stat}}/\sigma_{\mathrm{fit}}$ is obtained. The mean of these ratios $\langle \sigma_{\mathrm{stat}}/\sigma_{\mathrm{fit}} \rangle$ is $0.98 \pm 3.6\,\%$. This means that the error value on the temperature fit is statistically accurate within 3.6 %.

As a last test for the temperature fitting, a possible dependency of the fitted error to the simulated signal to noise ratio of the test data is examined. The dependency of the signal to noise level to the integration time is already known from section 4.1. Employing this, the signal to noise ratio will be shown as integration times. This change of variables is done, because integration time is a more intuitive

quantity than signal to noise ratios.

Again, for each integration time, the ratio $\sigma_{\text{stat}}/\sigma_{\text{fit}}$ is calculated. The mean of these ratios $\langle \sigma_{\text{stat}}/\sigma_{\text{fit}} \rangle$ is $1.01 \pm 4.0\,\%$. This means that the error value on the temperature fit is statistically accurate within $4.0\,\%$.

These two tests show that the error on the temperature fit is self-consistent.

7.2 Comparision with previous work

Noll et al. describe in [4] their work with the European Southern Observatory (ESO) at Cerro Paranal in Chile. The telescope is located at a height of 2,635 m, and $24\,°38'$ S, $70\,°24'$ W. It has four unit telescopes of 8.2 m diameter each[49]. This telescope has an astronomical echelle spectrograph, called XSHOOTER, which is able to measure all OH transitions that can be seen from the ground simultaneously [4]. Depending on the wavelength area (ultraviolet (UV), visible (VIS) or near infrared (NIR)) and the entrance slit widths, the resolution $\lambda/\Delta\lambda$ ranges from 3,300 to 18,200.

The most important wavelength region for comparison with this thesis is the NIR region. For the XSHOOTER, this area ranges from 1,020 nm to 2,480 nm. The imaging array is of the same type as in the NOTCam, a Hawaii 2RG array with 2,000 times 2,000 pixels. The gain was measured to be $2.12\,^{\text{electrons}}/_{\text{ADU}}$ [50].

Noll et al. used 343 spectra taken during 2009 and 2013. They also try to use these data to achieve measurements of the OH airglow. In their paper[4] they give their preliminary results. They studied fitted rotational and vibrational temperatures to 25 transitions from 8-2 to 9-7, including the eight transitions used in this thesis.

Noll et al. discussed a line selection. The line selection was tested by fitting a temperature to the spectra with different subsets of lines. With this technique, the unreliable lines were found and eliminated. For the nightly change in rotational temperature, Noll et al. found that it increases during the night. The intensity on the other hand is found to be decreasing in an average during all nights observed by them.

The spectrograph and telescope in use by Noll et al. is different from the NOTCam and NOT. Therefore, their work can only be compared to this thesis in parts. The line selection is a very important part in the data evaluation process. The number of reliable lines is at maximum eight for Noll et al. Therefore, the result on the temperature fit can change, if unreliable lines are included to the line selection. Single lines can be perturbed by atmospheric absorptions, overlapped by neighbouring transition lines or simply be not representative for the rotational temperature of the transition due to other reasons. Such lines should not be used. But the more lines are used, the more data points for the fit are available. It is therefore important that the line selection is done with care. In the following, the line selection of Noll et al. and the one presented in this thesis, will be compared.

Noll et al. use two strong base assumptions to narrow down the number of lines used. The first one is that lines coming from a level higher than $n = 4$ will not

be used following [28]. This assumption was also used in this thesis. It defines the edges of the spectra.

The second assumption they use is that only resolved lines will be used. For Noll et al. that means that nearly the whole Q and R-branches are not usable. In this thesis, the fitting was not done by comparing resolved peaks, but by directly fitting the whole spectrum. Since the model spectrum for the fitting can be unresolved, too, the unresolved peaks can be used as well. If the hights of two lines (a and b) are dependent on the temperature, the sum of these lines is still dependent on the Temperature[2].

In table 7.1, the remaining eight lines in the P-branch are shown. A one in the table means that this line is used in this thesis, a two means that it was used by Noll et al. in [4]. Most of the line selection is done similar in both works. The line selection for the transitions 3-1, 7-4 and 9-7 was exactly the same.

Transition	$P_2(1)$	$P_1(1)$	$P_2(2)$	$P_1(2)$	$P_2(3)$	$P_1(3)$	$P_2(4)$	$P_1(4)$
3-1	1,2	1,2	1,2	1,2	1,2	1,2		
4-2	1,2	1,2	1,2	1,2	1,2	2	2	
5-3	1	1,2	1,2	1,2	1,2	1,2	1	1
6-4		2		2				
7-4	1,2	1,2	1,2	1,2	1,2	1,2	1,2	1,2
8-5	1	1,2	1,2	1,2	1,2		2	2
8-6			1,2	1,2	1	1		1,2
9-7	1,2	1,2	1,2	1,2	1,2	1,2	1,2	1,2

Table 7.1: The P-branch lines used for the different transitions. A one in the table means that is was used in this thesis, a two means that the line was used by Noll et al.

The P-branch of the 6-4 transition is not inside the filter range of the NOTCam and can therefore not be used in this work, while it is possible for Noll et al. The high lines of the 4-2 transition are not used in this thesis because they lie on the edge between two subarrays of the NOTCam and are therefore not reliable. See as well figure 5.3 in section 5.2.

The line selection for the 8-6 transition in the work from Noll et al. and this thesis is very different. The main reason for rejecting lines in this thesis for this transition were NOTCam specific effects, which were discussed before in section 6.2. The spectrometer used in [4] did not show these effects. This difference in the spectrometers explains the difference in the line selection.

For the last two transitions, the 5-3 and 8-6 transitions, the work from Noll et al. had to reject lines. The reason for this rejection is that the temperature result changed when including these lines. This could not be reproduced for the NOTCam data. This can be due to lower signal to noise ratio at the NOT. With this lower signal to noise ratio, small changes in the fitted temperature can not be observed. Therefore, more lines were used here than in the work from Noll et al.

[2]In the extreme case, where all lines superpose into one line,all information would be lost after normalization. This extreme case is not sensible here and will not be discussed further.

In table 7.2, the temperature of the observation NCwb19 are shown, similar to table 6.3 in section 6.3. Additionally, the same data is shown, but this time using the line selection from Noll et al. The 6-4 transition could not be evaluated this way and is therefore missing, because none of the lines used from Noll et al. lie within the filter range of the NOTCam. Furthermore, the difference between the temperature results for both line selections are shown for each transition. The error on this difference was calculated as well.

	This thesis		Noll et al.		Difference	
Transition	T [K]	σ_T [K]	T [K]	σ_T [K]	ΔT [K]	$\sigma_{\Delta T}$ [K]
3-1	190.0	0.78	189.3	0.95	0.7	1.23
4-2	189.6	0.98	188.9	1.28	0.7	1.61
5-3	188.0	0.56	186.8	1.11	1.2	1.23
6-4	186.9	1.59	-	-	-	-
7-4	228.5	4.90	224.2	5.3	4.3	7.22
8-5	190.3	2.71	208.2	13.16	17.9	13.43
8-6	192.8	1.75	197.4	2.4	4.6	2.97
9-7	182.9	0.70	180.4	0.9	3.4	1.14

Table 7.2: Fit results compared with the line selections used before in chapter 5 and the line selection from Noll et al.[4]. The difference between the results for each transition is shown as well, together with the error on this difference.

The first four transitions, that are comparable are the 3-1, 4-2, 5-3 and 7-4 transitions. For these transitions, the differences between the temperature results for both line selections is smaller than the errors on this values. This says that these results are self-consistent. The 7-4 transition has large errors on the temperature results for both line selections, as the signal to noise ratio in the J band is smaller than in the other bands due to lower transition probabilities for the $\Delta v = 3$ sequence.

For 8-5 transition with the data from the NOTCam and the line selection from Noll et al., only 3 lines could be used. Therefore, the value of the temperature result has a very big error.

The results for the 8-6 transition are different from each other within 2σ. Since the line selection from Noll et al. only includes three lines and the line selection from this thesis includes only five lines, the results can easily be perturbed by random effects.

The last transition is the 9-7 transition. The difference of the temperature results only lies within 3 σ of the error. The difference in the line selection for this transition is that in this work lines from all the branches, P, Q and R, were used, while Noll et al. only used the P-branch lines.

To test whether this is a systematic deviation of the two line selections or just a random occurrence, the test was repeated for the other observations NCvi06. In none of the other observations this deviation could be observed. It is therefore assumed, that it is only a random occurrence.

In general, all the errors on the fitted values are smaller for the line selection used in this work. This is because the line selection employed here uses more lines for the fitting, since the fitting procedure presented above allows also fitting for unresolved lines.

Figure 6 in [4] shows as well a result, that was also observed here, that the 8-6 and the 8-5 transitions are of higher rotational temperature than the temperature profile would suggest. It remains a question for further research whether this effect comes from the fitting method, the spectroscopic parameters in HITRAN, or the OH airglow directly.

7.3 Comparison to the MSIS model

The Mass-Spectrometer-Incoherent-Scatter (MSIS) model is a model for neutral temperatures and densities in the atmosphere. The first version MSIS-86 was based on extensive data and analysis from A. E. Hedin et al. The newest version is NRLMSISE-00 (in the following reffered to as MSIS). For altitudes higher than 72.5 km, it uses data from space shuttle flights and incoherent scatter results[3].

In comparison to the CIRA86 model, the MSIS model is not climatology, but takes short term effects into account, if they are in the measurements that constitute the model. It is part of the Community Coordinated Modeling Center (CCMC) at NASA.

For a given position on earth, a date and time, the model yields a temperature profile from ground up to 1,000 km. It is a useful tool for this thesis for comparison of the observations. All three observations with available H, J and K-band will be compared to the model. These three observations are NCwb19, NCvi06 4 and NCvi06 5. Their local time of observation can be found in table 6.1.

The altitudes of the emissions are not known from the NOTCam data. For these altitudes, averaged values will be used. For the distance between two emission altitudes, this was already used in section 6.3.1. Baker and Stair showed in [22] that the average altitude for the 3-1 transition is 87 km. This will be used. The average spacing between the emission from two neighbouring v' levels is 0.5 km[48].

It is important to notice that these altitudes are climatological values and not measured or modelled values for the observation time and place. In following work, a OH model could be used to use the MSIS atmosphere to model the OH as well and achieve better values for these altitudes.

In figure 7.3, the MSIS model data and the measured temperatures of the observations NCwb19, NCvi06 4 and NCvi06 5 are shown for these altitudes. The model data are shown as a line, while the data points from the observations are shown with their statistical errors. The average altitudes of the transitions from v' are stated in the figure.

The $v' = 7$ transition is very weak in intensity as it is in the J-band with $\Delta v = 3$. It was observed before that this transition is very unprecise. This transition only lies for the NCvi06 4 observation inside the shown area. The two transitions from $v' = 8$ yield a too high temperature for all three observations. This deviation was observed before for the NCwb19 observation.

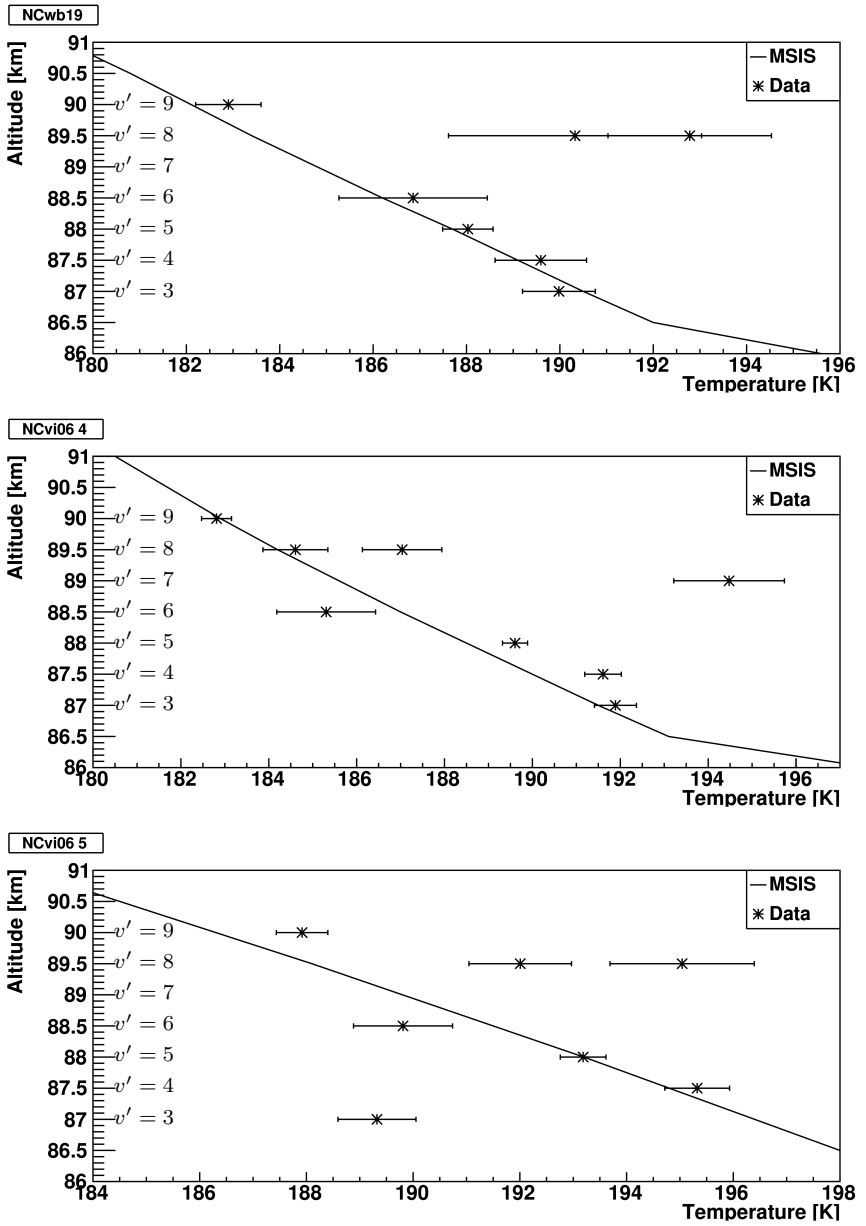

Figure 7.3: Comparison with the MSIS model. The model was calculated for the position of the NOT at the averaged time of observation. The v' value is stated for each altitude.

The observation NCwb19 was already shown this way in figure 6.4. There, the temperature profile was fitted. Here in figure 7.3, the temperature profile is the independent model from MSIS. It can be seen that the MSIS model fits the five datapoints used in figure 6.4. These transitions are the 3-1, 4-2, 5-3, 6-4 and 9-7 transitions.

For the observation NCvi06 4, the 7-4 transition can be seen far off the model temperature profile. The five transitions 3-1, 4-2, 5-3, 6-4 and 9-7 scatter around the temperature profile and agree to it as well in the overall tendency.

For the last observation, the 4-2, 5-3, 6-4 and 9-7 transitions also scatter around the MSIS model temperature profile. The 3-1 transition however shows a significant deviation. For this transition, all three available pictures from the ABBA scheme show the same deviation. The fit worked for all three spectra and the residuals did not show any problems. It is therefore likely that the band was perturbed. Since the other transitions from the H-band (the 4-2, 5-3 and the 6-4 tansitions) do not show this deviation, it is unlikly to be a systematic effect of the data evaluation. A very locally confined atmospheric perturbation can form this deviation.

The results presented in this work fit to the MSIS model in nearly all points. This is true even though the the altitudes of the emissions come from climatological values and are not directly modelled or measured for the nights of the observations. This demonstrates that this method yields reliable results that are consistent with the MSIS model.

Chapter 8

Further research

The aim of this thesis was to give a proof of concept. The basic idea was to demonstrate that quantitative observations of OH airglow can be performed with the NOT. In the previous chapters it was shown, that atmospheric temperatures in the MLT region can be derived from standard observations from the NOTCam. These results were shown to be consistent with atmospheric models and other observations to within the small uncertainties of the NOTCam observations.

The next question is then, what can be done with this technique? In this chapter, I will outline three scientific questions in detail, that can be answered with NOTCam observations. It will be shown that these projects are entirely possible and how they can be achieved. First in section 8.1, it will be shown that not only the rotational temperature can be fitted from the data, but also the vibrational level population N_o. Knowing N_o, one can calculate in a second step the OH heating rates. This calculation will be shown in section 8.2. In section 8.3, the possibilities arising with dedicated telescope time will be discussed. An experiment to measure atmospheric waves with telescope time will be simulated. The aim of this simulation is to achieve the best observation parameters.

The NOTCam has been mounted to the NOT for near-IR spectroscopy measurements for, on average, 15 % of the time during the last 14 years. Figure 8.1 shows the distribution of dates between November 2007 and March 2014 when the NOTCam was used for long-slit spectroscopic observations. Good seasonal coverage is achieved from data recorded throughout the year.

All data older than one year (the proprietary period at the NOT) are available in the NOT data archive. Standard star observations are available immediately. Fig. 8.2 shows histograms of the total number of spectroscopic observations taken in the J, H and K bands for each hour during the night. Good coverage across all hours of darkness is achieved in each wavelength region.

With such a good coverage, it is also possible to study the temperature climatologically. The temperature can be studied in short and long term changes for this region of the atmosphere. This work can then be added to a study of the temperature changes at a higher latitude, where the incidence of energetic particle precipitation into the atmosphere is higher. The combined result will give insights

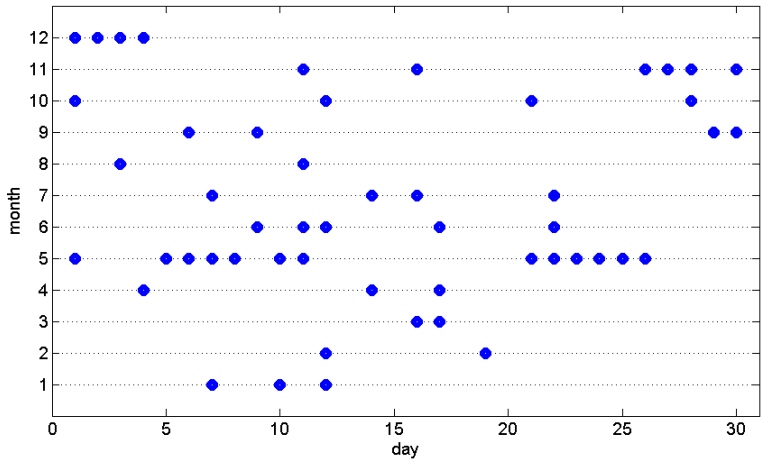

Figure 8.1: Dates between November 2007 and March 2014 when the NOTCam has been mounted at the NOT and making spectroscopic astronomical observations. The figure was already shown as figure 3.1 in chapter 3.

of the drivers of the long term changes.

The NOT will profit from these atmospheric studies as well. For astronomical observations, a knowledge of the background is very important. One dominant part of this background for NIR measurements is the OH airglow. In parallel with the work, described in this chapter, the background intensity will be quantified for astronomical studies. This work will help in planning future near-infrared/optical instrumentation and in optimising observing schedules at the observatory.

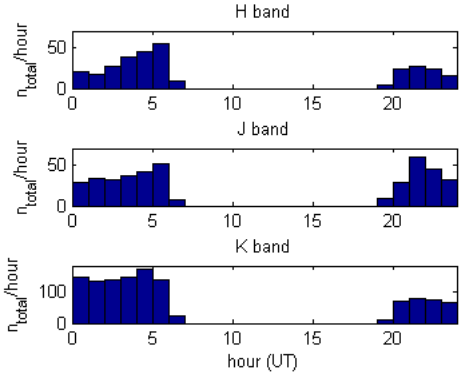

Figure 8.2: Total number of spectroscopic data frames recorded in each hour and each wavelength region with the NOTCam between November 2007 and March 2014.

8.1 Vibrational level population

After fitting the rotational temperatures in the previous chapters, one can also have a closer look on the second free parameter of equation 2.9, the vibrational level population N_o. A knowledge of N_o opens up more possibilities for questions. One example for such a question are the OH heating rates, which will be discussed in section 8.2

8.1.1 Fitting

In the temperature fits so far, the spectra were normalized. The normalization makes the spectra independent of N_o. Indeed it the normalization constant directly related to N_o. Given the integral under the filtered synthetic spectrum with $N_o = 1$ as I, the normalization factor is IN_o. I is a very small number. For example for a 5-3 transition with a rotational temperature of 200 K, it is approximately 1×10^{-51} . At the same time, N_o is a big number around 1×10^{50} . This makes this method of finding N_o numerically instable. Another method is therefore proposed here.

Going back to the non-normalised spectrum but knowing accurately the rotational temperature, another fit is now executed. This fit has N_o as a free parameter. The synthetic spectra for fitting are no longer normalized[1], but they have the rotational temperature as fixed parameter. Since the value on N_o is varying strongly, the N_o is not fitted directly, but rather x, where $N_o = 10^x$.

The fit for the observation NCwb19 can be found in figure 8.3. The result is 60.51 ± 0.001 for x. This gives a value for N_o of $10^{60.51}$ with an error of 0.2 %. The graph looks of course very similar to figure 5.7 of the temperature fit. The difference between the graphs in figure 8.3 and figure 5.7 is only the scaling on the y-axis. The residual looks exactly the same as figure 5.8 except for the y-scale. It is therefore not presented here again. The results for the data available in this thesis can be found in table 8.1. The errors on these values are found to be very small. There are two transitions with $v' = 8$. In theory, they should have the same N_o value. Here, they differ a little from each other. However, it was already discussed for the temperature fit, that the 8-5 transition yields bad results. The deviation is therefore no issue.

As in section 7.1, this fit can be tested. Synthetic test data were created for different values of the integration time N_o and T_{rot} . Neither the fitted value of N_o, nor the error on this value showed dependencies. This shows that the fitting routine is stable. This is not suprising, as only the sclaing factor is fitted. This routine is very stable.

The two parameters in equation 2.9 are not independent of each other. As a second step in future research it is therefore proposed to use a two dimensional

[1] It is important to notice that the spectrum is not yet absolutely calibrated in intensities. The density is therefore only a relative number. To calibrate the spectrum, the measurement of standard stars has to be used. With these, the spectrum can be calibrated to intensity. From there, one can also calculate the real intensity by multiplying with $h\nu$. This step is proposed for further research. Here, it is shown, that the fitting as it is works. The calibration is standard for astronomical spectroscopy.

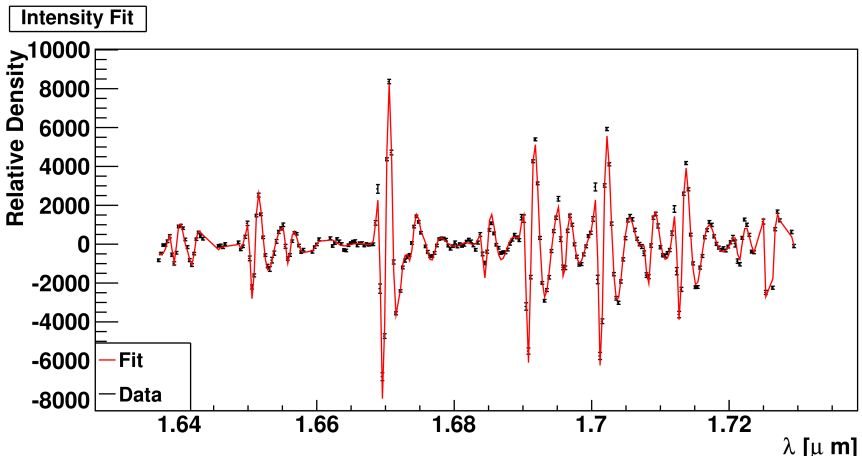

Figure 8.3: Fit of N_o to the not normalized spectrum with the rotational temperature fixed. The result is $10^{60.51}$ with an error of 0.2 %.

Transition	N_o	σ_{N_o}
3-1	40.317	0.001,2
4-2	50.755	0.001,3
5-3	60.516	0.001,0
6-4	74.460	0.003,2
7-4	64.940	0.005,8
8-5	83.868	0.004,9
8-6	79.933	0.002,3
9-7	93.800	0.001,0

Table 8.1: The fitted results for the N_o for the observation NCwb19. The bands used can be found in table 6.2 and figure 6.2 and 6.3.

fitting algorithm to fit both parameters T_{rot} and N_o at the same time. This has been done by others before, for example by Kvifte[51].

8.1.2 Intensity - time dependency

As already seen in previous work[52] and discussed in section 2.2, the intensity of the OH airglow has a typical development over a night. This development can also be shown with the observations NCvi06. The intensities, in measures of relative N_o, were fitted and plotted in figure 8.4. Here, the intensities were normalised such that the intensity of the first data point of the night (around 10 s after midnight) becomes 1.

This was done again for the 8-6 and the 9-7 transitions. Only these transitions are available over the course of the whole night. Both profiles qualitatively have the same development with a small, quick variation at midnight and an increase at

the end of the night.

Again, the variation is large in comparison to the statistical errors from fitting, showing that the change is not just a statistical relic.

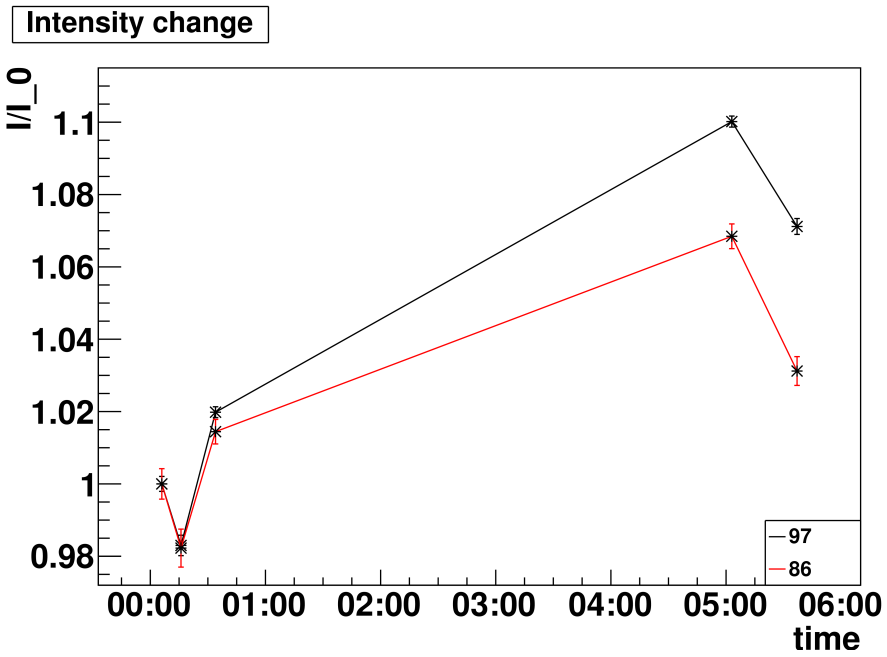

Figure 8.4: Development of the relative intensity in the course of a night. The observations NCvi06 were used for this plot. The intensities are normalized to the intensity of the beginning of the night for each transition. Only the 8-6 and the 9-7 transitions were available over the whole course of the night.

One can see that the intensity follows a typical change, as discussed in section 2.2 and shown in figure 2.3. This typical change is to be higher at the beginning of the night, lower in the middle and increases shortly before sunrise.

8.2 OH heating rates

The integrated intensity of each OH vibrational band v (normalised for integration time) gives a measure of the total radiative loss-rate from v during the observation. The concentration of OH in each of the vibrational bands OH(v) is discussed in [31]. A formula to calculate this concentration was already stated in equation 2.10 to be:

$$[\mathrm{OH}(v)] = \frac{f_v P_C \sum_{v'} A_{v'\to v}[\mathrm{OH}_{v'}] \sum_{v'} k_{v'\to v}[\mathrm{M}][\mathrm{OH}_{v'}]}{\sum_{v'} A_{v'\to v} \sum_{v'} k_{v'\to v}[\mathrm{M}] + k'_c[\mathrm{O}]}, \tag{8.1}$$

where P_C is the production rate of vibrational excited OH (reaction (2.5)) and f_v is the fraction of production of state v. The other two terms in the numerator describe indirect sources of OH(v): spontaneous emissions, and collisional deactivation processes ($k_{v' \to v}$ is the quenching rate) from vibrational states with higher vibrational energy. The denominator consists of radiative, collisional and chemical loss mechanisms.

If the number density of at least one vibrational mode of OH and all its productions and losses are known, the heat deposited into the mesopause by the $H + O_3$ reaction can be derived directly from the [OH(v)] measurements. The v=9 vibrational level is the highest one reached from the $H + O_3$ reaction (reaction 2.1). Therefore, the 9-7 transition is the ideal candidate to measure the heating rates ($^{\mathrm{d}\,\Theta}/_{\mathrm{d}\,t}$). This choice was also outlined in [31].

Such data are readily available from the 9-7 OH vibrational band resolved in the many K-band spectroscopic data frames recorded with the NOTCam (see figure 8.2 and 6.3).

8.3 Possible dedicated observations

As discussed, the results of this work uses only by-products from astronomers day-to-day work. However, as the observations NCvi06 1, 2 and 3 showed, this data as a by-product can yield incomplete observations, which can result in systematical errors. The natural question then is what could be achieved if one could directly use the telescope with parameters optimised for atmospheric observations.

The NOTCam could be used to obtain a high temporal resolution measurement of the atmospheric temperature changes during the course of its dedicated observation time. The most dominant short-term changes would be caused by atmospheric waves. The frequencies of atmospheric waves can range from high frequence infrasound with 0.05 Hz to gravitational waves with periods up to hours. These waves can be generated from various mechanisms. One example is gravity waves which occur when a parcel of air is displaced and then falls back to equilibrium position due to gravity. As it has kinetic energy it will overshoot and begin to oscillate, when reaching equilibrium. The initial displacement can happen when an air parcel is driven up a mountainside by winds. These gravity waves propagate up into the atmosphere and can reach the MLT region [7].

The atmosphere is strongly coupled through the waves and various atmospheric effects based on the waves (see for example [7]). A measurement of the waves in high altitude could reveal much about the atmospheric coupling.

The possibilities for such a measurement with the NOTCam will be discussed in this section. To quantify this discussion, the measurement will be simulated, based on the work presented in this thesis so far. The simulation is done in three steps. The first step is to simulate a single observations with the aim to obtain a relationship between the expected error on the temperature fit from this observation and the integration time assumed for the simulation.

The second step is to simulate a measurement of a wave with a given frequency over time. For this, timely separated measurements of an oscillating temperature

will be simulated. The quality of the measurement will be found dependent on the simulated integration time.

As the last step, the magnitude of the wave, its frequency and the integration time for the simulation will be varied, to obtain the best integration time for a given wave in section 8.3.3.

8.3.1 Expected error on temperature fit for a single observation

First the question will be answered, how precise a single temperature fit can be depending on the integration time of the observation. It is already approximately known, how high the background noise level is to be expected for a given integration time from figure 5.5. This noise measurement assumes that the signal noise is the dominant one. This approximation will be used in the following. This observation assumes only one measurement per observation, the ABBA scheme is not necessary for this measurement.

For a given integration time, the observation can be simulated. Synthetic data are created with the background noise level according to figure 5.5. A temperature fit can be executed for these synthetic data. The result is a temperature and the error on this value. To minimize the effect of randomly occurring events, this procedure is done 10 times and the average of the errors on the temperature fit is calculated. This averaged error is called σ_T. The standard deviation on σ_T was also calculated from the 10 repetitions.

Figure 8.5 shows this procedure done for integration times between 1 s and 50 s. The values of σ_T stabilize quickly for low numbers of repetitions for every integration time. For short integrations times, σ_T becomes rapidly bigger.

The limits of this function are known. For the integration time $t \to 0$ the σ_T is expected to approach infinity. This can be verified with the figure 8.5. For $t \to \infty$, σ_T is expected to go to 0, since the noise will go to 0 and the test data will be a perfect model again. This limit can also be found in figure 8.5.

In reality, even with infinite t, the noise level will not drop to zero, but stabilize on a fixed, small and positive value due to the constant read-out noise of the detector and random occuring effects as cosmic rays[2]. This stabilization value can be different from observation to observation. This constant offset was found by comparison to the available transitions and integration times to be on average 0.2 K. It is important to note that this value is very unstable since it will change from picture to picture and transition to transition.

It was found that the data points from figure 8.5 can be fitted with the function

$$\sigma_T(t) = {}^{a}/\sqrt{t},\ a \in \mathbb{R}^+. \tag{8.2}$$

[2]All integration times considered here are small. That means that the cosmic rays are not a dominant effect. For infinite integration time, the measurement would have cosmic rays on ever pixel. This case is not sensible here and will not be consered.

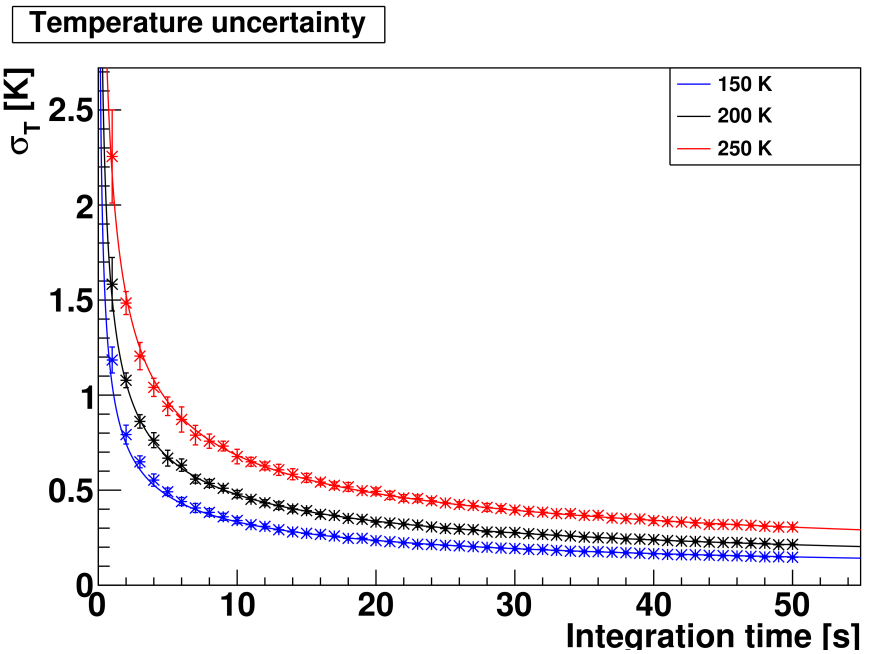

Figure 8.5: Expected uncertainty on temperature fits for different integration times. The dependency is shown for the temperatures 150 K, 200 K and 250 K.

One has to keep in mind that this is only an empirical relationship. However, it is shown in figure 8.5, that the approximation is good. It will be used in the following.

This dependency was found explicitly for the three temperatures 150 K, 200 K and 250 K, and varies slightly as a function of temperature. The parameters a found are listed for the different temperatures in table 8.2. In the following an atmospheric rotational temperature of 200 K will be assumed. The a value for this temperature will be used. This temperature is approximately the temperature of all evaluated observations in this thesis and in a good approximation for an average temperature from the CIRA86 model for the latitude of the observations.

Temperature [K]	a $[K\sqrt{s}]$	σ_a $[K\sqrt{s}]$
150	1.053	4.5×10^{-3}
200	1.603	7.2×10^{-3}
250	2.160	9.8×10^{-3}

Table 8.2: The parameter a for different temperatures with its error.

8.3.2 Expected signal to noise level for wave observations

With figure 8.5, the expected accuracy of a temperature measurement for a given integration time is known. This raises the question of how accurately an atmospheric wave could be measured with the NOT.

Assuming an amplitude of the wave be 1 % and 4 % and observed frequency between 3.5×10^{-5} Hz (equal to a period of a third of a day (8 h)) and 0.03 Hz (equal to a period of 30 s). These numbers are based on the survey from Nielsen et al.[53]. They measured the occurrence rate of atmospheric waves for different wave frequencies. Their result can be found in figure 8.7(b). As an example it is assumed that one hour of telescope time is available.

The measurement can now be simulated. For a given integration time t and a relative wave amplitude $\frac{\Delta T}{T}$ a frequency f will be assumed. For this integration time t, the error on a temperature measurement can be estimated with equation 8.2. A wave will now be simulated with $\frac{\Delta T}{T}$ and f and perturbed with white, Gaussian noise of $\sigma = \sigma_T$ and a random constant phase shift. The distance on the time-axis between two data points is then the integration time t plus the downtime Δt_{down} of the telescope for the image readout. The latter is 10 s [37].

This artificial data can be fitted by a wave with unknown amplitude p_0, frequency p_1 and constant phase shift p_2. The fitted function is then:

$$f(x) = p_0 \sin(p_1 x + p_2) \tag{8.3}$$

The fit yields the wave amplitude and frequency and the constant phase shift, as well as the errors on these values. The error on the amplitude ΔT, which will be called $\sigma_{\Delta T}$, will be discussed below.

Three examples for this fit can be found in figure 8.6. For smaller t, the observation yields many data points with large errors. On the other hand, with large t, the error becomes smaller from figure 8.5, but the number of data points at which the wave is sampled deceases. If $t \ll 1/f$ does not hold, the temperature will change significantly during the integration time. The temperature measurement will then have a larger error and the value for the temperature will be averaged over the range of temperatures during t. In the extreme case of $t = 1/f$, the measured temperature becomes the average temperature with a large error. This effect is also included in the simulation.

It is intuitive that an integration time in the middle is therefore the best. At this point, this optimal integration time t_{opt}, can also be dependent on the wave frequency or amplitude. As a criterion of the quality of the observation, the obtained signal to noise ratio of the measured wave amplitude is chosen. This ratio $\Delta T/\sigma_{\Delta T}$, is the signal to noise ratio of the amplitude measurement. At the same time, this ratio is the confidence interval [3] for this wave not to be a constant temperature with random noise.

[3] and thereby the probability

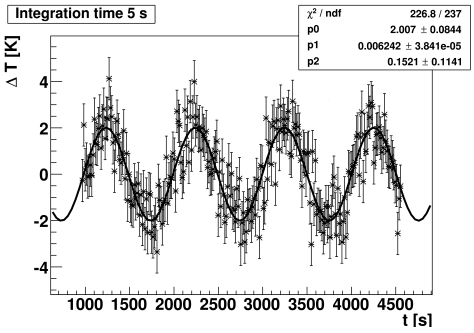

(a) Integration time 5 s

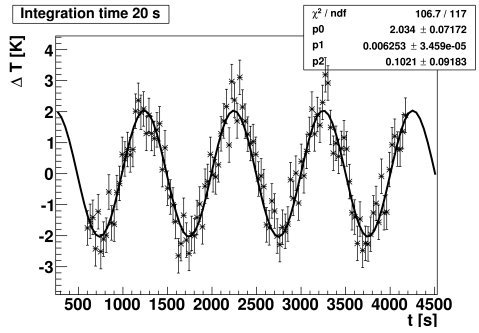

(b) Integration time 20 s

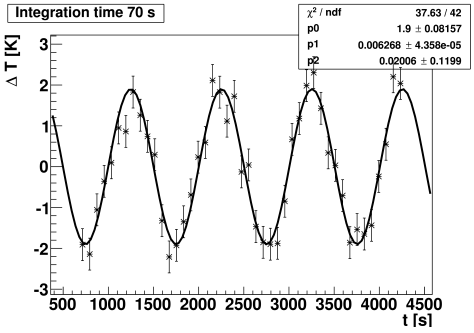

(c) Integration time 70 s

Figure 8.6: Example simulated atmospheric waves with $\frac{\Delta T}{T}$=1 % and f=1 × 10^{-3} Hz. On the x axis, the ongoing time during the observation is shown. The waves in the simulation are observed with different integration times t. The shorter t, the more data points with bigger error margin and vice versa.

8.3.3 Discussion of the optimal integration time

The result over a large range of variations for t and f can be found in figure 8.7(a). Here, a relative amplitude of 1 % was assumed. Note that both the x and the y axes are logarithmic. For very low frequencies, the period becomes larger than the observation time and the fit quality, drawn on the colour axis, goes down, because the fit becomes more and more difficult. On the other side, for higher frequencies, the number of points per wave period becomes smaller. It was found that the fit is only satisfactory if the number of data points in one period is at least four. Since only three of these data points have to be read out during the period, the minimum period $p_{\min} = 4t + 3\Delta t_{\text{down}}$. If this criterion is not fulfilled, no fit can be achieved. This creates the cut-off or Nyquist frequency, dependent on the integration time t.

The optimal integration time was found to be 20 s and indeed independent from the wave frequency. This of course only holds for frequencies smaller than the Nyquist frequency. For bigger frequencies the largest integration time possible is best.

In figure 8.7(b), the relative occurrence rate of atmospheric waves dependent on their frequencies is shown. This measurement was done by Nielson et al.[53] over Halley in Antarctica. Figure 8.7 demonstrates that the observes waves have frequencies lower than the Brunt-Väisälä which in turn is much lower than the Nyquist frequency for these observations.

The same test was also done for different wave amplitudes. For example, the result for $\frac{\Delta T}{T}$ =4 %, can be found in figure 8.8. Only the scale of the colour axis changes, as the amplitude becomes four times bigger but the error one the amplitude measurement stays the same. The optimal integration time stays unchanged.

This opens up the possibilities to make high signal to noise wave measurements over frequency ranges currently unavailable to more convetional ground based instrumentation (for example [54]).

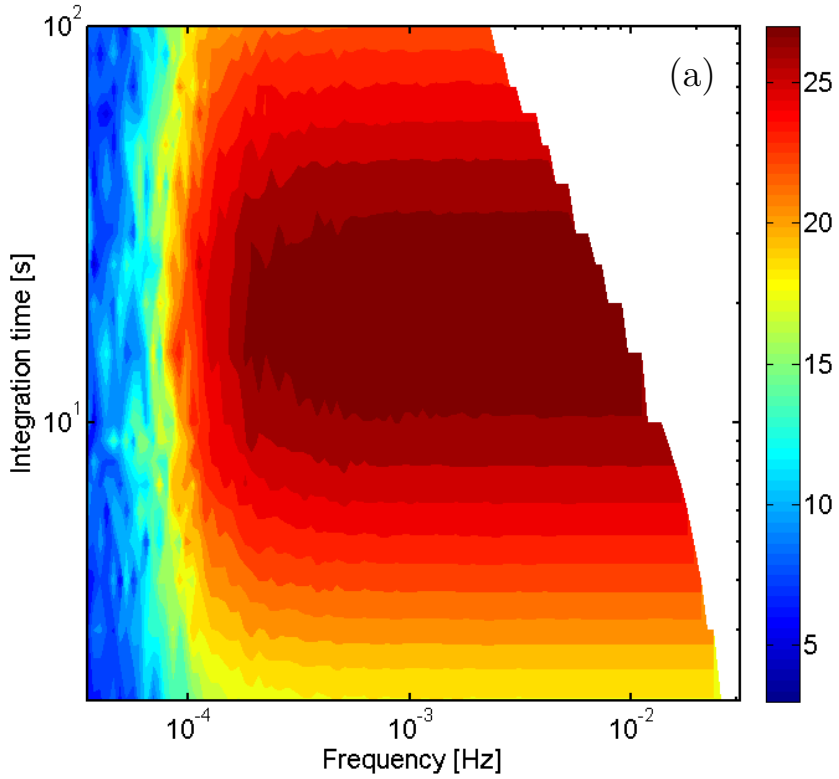

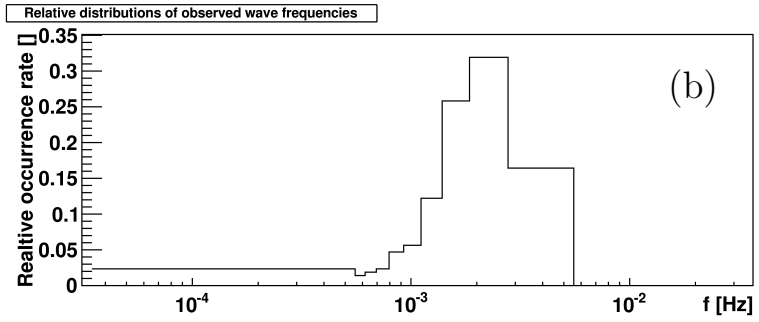

Figure 8.7: (a) Expected signal to noise ratio of an observed wave with a relative amplitude $^{\Delta T}/_{T} = 1\,\%$. A one hour observation time was assumed with readout times between the images of 10 s. The error estimate is based on the observed 9-7 transitions.
(b) Expected relative number of waves observed from [53].

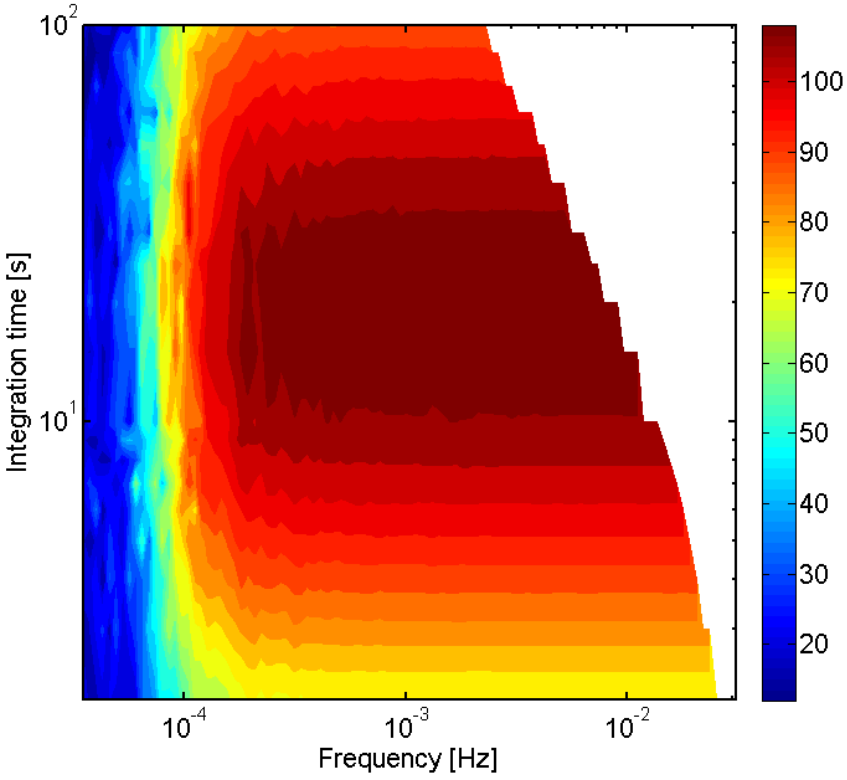

Figure 8.8: The same procedure as presented in figure 8.7, but with a relative wave amplitude $\frac{\Delta T}{T}$ =4 %.

Chapter 9

Conclusion

The topic of this thesis is to evaluate the data from astronomical spectroscopy experiments executed with the NOT. In chapter 1, it was discussed how and why the results obtained here are important. The IPCC reports, and the maximal altitudes of the models within them, were considered, and it was seen that the MLT has increasingly become a region of interest.

After a short theoretical introduction in chapter 2 an overview over the NOT and the NOTCam was given in chapter 3. Chapter 4 listed effects which are particular to the NOTCam . The solutions for the reduction challenges where given and discussed in chapter 5. An approximate noise measurement was presented in figure 5.5 and the bending of the OH lines due to the optics inside the NOTCam was evaluated. A mapping was created to straighten the lines out for a later creation of a normal spectrum. The line shape for the OH lines was found to be a superposition of several Gaussians, where the centre of the superposing Gaussians vary over the width of the line. This can be approximated as a Gaussian with a 4 % wider width.

An example of the data reduction was shown using the NCwb19 observation in chapter 5. The reduction was done by the help of IRAF, a standard tool for astronomers, and by creating an effective and easy to use programming framework, that could solve the problems that are unique to the atmospheric lines observed by the NOTCam. With the help of the HITRAN line-parameter listing, a mask could be created to detect an overlap of neighbouring transitions and thereby to define the lines suitable for fitting. The rotational temperature was fitted with a small error margin for integration times as short as 10.8 s. For this, the spectrum was filtered to exclude the low frequency perturbations as well as any constant offsets. The fitting itself was not done by comparing the relative peak heights, but by comparing the spectrum to a synthetic spectrum with varying parameters. This made it possible to use unresolved lines as well.

The results were presented in chapter 6. First, the available lines in the transitions were discussed. An overview of the transitions was given in the figures 6.2 and 6.3. Two dependencies of the temperature were shown. First, the dependency of the temperature to the altitude, so the temperature profile. Secondly, the de-

velopment of the temperature over the course of a night, so the temperature-time dependency.

In chapter 7, it was shown that the routines yielded self-consisten results. For this, synthetic test data were created and evaluated with the routine. It was shown that the fit results and the errors on these results are statistically accurate to within approximately 4 %.

Afterwards, this work was compared to the work of Noll et al.[4]. The line selection was here of special interest. It was found that it differed little in the P-branch due to different spectrometers. Different spectrometer filters and the transition between two subarrays of the NOTCam were the most reasons. Additionally, Noll et al. had to reject a few line in the 5-3 and the 8-6 transitions, as they did not yield consistent temperatures. This could not be reproduced for the NOTCam data. This difference can be due to different noise levels and spectrometer accurancies. Since the routines presented in this thesis are capable of fitting unresolved lines as well as resolved ones, the R and Q-branches could be used, too, leading to smaller error margins and higher fit stability.

The results were also compared to the MSIS model. It was found that the most results are in agreement with the model. However, as in the work from Noll et al., it was found that the lines from $v' = 8$ yield an anomalously high temperature. Whether this effect is intrinsic in the atmosphere, due to the evaluation routines or is a product of the spectroscopic parameters listed in HITRAN is a matter for further research. The 7-4 transitions were found to be very unaccurate since they are in the J-band with a transition of $\Delta v = 3$ and therefore low in intensity. Therefore, this transition is easily perturbed and does not yield consistent temperature results. The 3-1 transition of the NCvi06 5 observation was found to be inconstistent with the MSIS model. It is not clear, what causes this deviation. Very localized wave perturbations in the atmosphere can be the reason.

This work leads directly to a number of further research topics. Possibilities were discussed in chapter 8. First, the vibrational level population N_o was discussed to be directly connected to the normalization factor from the temperature fit. For higher numerical stability, N_o was fitted as well as the rotational temperature. It was proposed to unify the two fits into one multidimensional fit in further research.

The development of N_o over the course of a night could be found and discussed with the observations NCvi06. After a discussion of the value of the NOTCam data and possible evaluations for OH heating rates, an observation with dedicated telescope time was considered. An expected error of a temperature measurement was found to be dependent on the chosen integration time of the NOTCam. With this dependency, an atmospheric wave could be simulated with the purpose to find the optimal integration time for a wave observation. This was indeed found to be wave frequency and wave amplitude independent[1]. The value of 20 s was found to be the optimal integration time for best observation results.

This work, as presented here, opens up possibilities to evaluate archived data from telescopes like the NOT and even to execute observations with telescopes for the purpose of atmospheric OH and MLT physics. For this, the needed evaluation

[1] except for the Nyquist frequency

software and methods are presented, as well as a first consideration of telescope parameters.

Bibliography

[1] Ipcc webpage. `http://www.ipcc.ch/`. Accessed: 2015-05-03.

[2] L.S. Rothman, I.E. Gordon, Y. Babikov, A. Barbe, D. Chris Benner, P.F. Bernath, M. Birk, L. Bizzocchi, V. Boudon, L.R. Brown, A. Campargue, K. Chance, E.A. Cohen, L.H. Coudert, V.M. Devi, B.J. Drouin, A. Fayt, J.-M. Flaud, R.R. Gamache, J.J. Harrison, J.-M. Hartmann, C. Hill, J.T. Hodges, D. Jacquemart, A. Jolly, J. Lamouroux, R.J. Le Roy, G. Li, D.A. Long, O.M. Lyulin, C.J. Mackie, S.T. Massie, S. Mikhailenko, H.S.P. Müller, O.V. Naumenko, A.V. Nikitin, J. Orphal, V. Perevalov, A. Perrin, E.R. Polovtseva, C. Richard, M.A.H. Smith, E. Starikova, K. Sung, S. Tashkun, J. Tennyson, G.C. Toon, Vl.G. Tyuterev, and G. Wagner. The HITRAN2012 molecular spectroscopic database. *Journal of Quantitative Spectroscopy and Radiative Transfer*, 130:4–50, November 2013.

[3] J. M. Picone. NRLMSISE-00 empirical model of the atmosphere: Statistical comparisons and scientific issues. *Journal of Geophysical Research*, 107(A12), 2002.

[4] S. Noll, W. Kausch, S. Kimeswenger, S. Unterguggenberger, and A. M. Jones. OH populations and temperatures from simultaneous spectroscopic observations of 25 bands. *Atmos. Chem. Phys.*, 15(7):3647–3669, April 2015.

[5] D. Qin M. Manning Z. Chen M. Marquis K. B. Averyt M. Tignor Solomon, S. and M. L. Miller (eds.). *Climate Change 2007: The Physical Science Basis. Contribution of Working Group I to the Fourth Assessment Report of the Intergovernmental Panel on Climate Change*, chapter TS, page 1–996. Cambridge University Press, Cambridge, United Kingdom and New York, NY, USA, 2007.

[6] T.F. Stocker, D. Qin, G.-K. Plattner, L.V. Alexander, S.K. Allen, N.L. Bindoff, F.-M. Breon, J.A. Church, U. Cubasch, S. Emori, P. Forster, P. Friedlingstein, N. Gillett, J.M. Gregory, D.L. Hartmann, E. Jansen, B. Kirtman, R. Knutti, K. Krishna Kumar, P. Lemke, J. Marotzke, V. Masson-Delmotte, G.A. Meehl, I.I. Mokhov, S. Piao, V. Ramaswamy, D. Randall, M. Rhein, M. Rojas, C. Sabine, D. Shindell, L.D. Talley, D.G. Vaughan, and S.-P. Xie. *Climate Change 2013: The Physical Science Basis. Contribution of Working Group*

I to the Fifth Assessment Report of the Intergovernmental Panel on Climate Change, chapter TS, page 1–1535. Cambridge University Press, Cambridge, United Kingdom and New York, NY, USA, 2013.

[7] Rosmarie J. de Wit. *Quantifying the influence of the stratosphere on the mesosphere and lower thermosphere*. PhD thesis, Norwegian University of Science and Technology, 2015.

[8] Roy W. Spencer, John R. Christy, and Norman C. Grody. Global Atmospheric Temperature Monitoring with Satellite Microwave Measurements: Method and Results 1979–84. *Journal of Climate*, 3(10):1111–1128, October 1990.

[9] Daniel R. Marsh, Anne K. Smith, Martin G. Mlynczak, and James M. Russell. Saber observations of the oh meinel airglow variability near the mesopause. *Journal of Geophysical Research: Space Physics*, 111(A10):n/a–n/a, 2006.

[10] R.Earl Good. Determination of atomic oxygen density from rocket borne measurement of hydroxyl airglow. *Planetary and Space Science*, 24(4):389 – 395, 1976.

[11] S. M. Smith, J. Baumgardner, C. J. Mertens, J. M. Russell, M. G. Mlynczak, and M. Mendillo. Mesospheric OH temperatures: Simultaneous ground-based and SABER OH measurements over Millstone Hill. *Advances in Space Research*, 45(2):239–246, January 2010.

[12] The atmosphere - origin and structure. `http://www.ux1.eiu.edu/~cfjps/1400/atmos_origin.html`. Accessed: 2015-04-23.

[13] Georg Witt. Height, structure and displacements of noctilucent clouds. *Tellus*, 14(1):1–18, February 1962.

[14] AnneK. Smith. Global dynamics of the mlt. *Surveys in Geophysics*, 33(6):1177–1230, 2012.

[15] Anne K. Smith. Physics and chemistry of the mesopause region. *Journal of Atmospheric and Solar-Terrestrial Physics*, 66(10):839 – 857, 2004. Upper Atmosphere Tutorials from the 2001 Joint {CEDAR} {SCOSTEP} Meeting.

[16] Editor D. Rees. Cospar international reference atmosphere 1986 part l. thermospheric models, 1988. Advances in Space Research, Vol. 8, No. 5/6, Pergamon Press, Oxford and NY.

[17] J. J. Barnett K. Labitzke Rees, D. Cira 1986, cospar international reference atmosphere, part ii: Middle atmosphere models, 1990.

[18] CCMC: Community Coordinated Modeling Center. `http://ccmc.gsfc.nasa.gov/`. Accessed: 2015-04-23.

[19] G.G. Sivjee. Airglow hydroxyl emissions. *Planetary and Space Science*, 40(2–3):235 – 242, 1992.

[20] P.J. Espy and J. Stegman. Trends and variability of mesospheric temperature at high-latitudes. *Physics and Chemistry of the Earth*, 27(6-8):543–553, 2002.

[21] F. Sigernes, N. Shumilov, C. S. Deehr, K. P. Nielsen, T. Svenøe, and O. Havnes. Hydroxyl rotational temperature record from the auroral station in adventdalen, svalbard. *Journal of Geophysical Research: Space Physics*, 108(A9):n/a–n/a, 2003.

[22] Doran J. Baker and A. T. Stair Jr. Rocket measurements of the altitude distributions of the hydroxyl airglow. *Physica Scripta*, 37(4):611, April 1988.

[23] Endre Asheim Hennum. A new algorithm for remote sensing mesopause temperatures using the hydroxyl airlgow, 2013.

[24] N. Parihar, A. Taori, S. Gurubaran, and G. K. Mukherjee. Simultaneous measurement of OI 557.7 nm, O2 (0, 1) Atmospheric Band and OH (6, 2) Meinel Band nightglow at Kolhapur (17° N), India. *Ann. Geophys.*, 31(2):197–208, 2013.

[25] A. B. Meinel, II. OH Emission Bands in the Spectrum of the Night Sky. II. *Ap.J.*, 112:120, July 1950.

[26] B. H. Bransden and C. J. Joachain. *Quantum Mechanics*. Addison-Wesley, Harlow, England ; New York, 2 edition edition, February 2000.

[27] Jr. P.J. Espy Pendleton, W.R. and M.R. Hammond. Evidence for non-local-thermodynamic-equilibrium in the oh nightglow, j. geophys. res., 98, 11567-11579, 1993.

[28] P C Cosby and T G Slanger. OH spectroscopy and chemistry investigated with astronomical sky spectra. *Canadian Journal of Physics*, 85(2):77–99, February 2007.

[29] Martin G. Mlynczak and Susan Solomon. A detailed evaluation of the heating efficiency in the middle atmosphere. *Journal of Geophysical Research: Atmospheres*, 98(D6):10517–10541, 1993.

[30] Martin G. Mlynczak. A new perspective on the molecular oxygen and hydroxyl airglow emissions. *Journal of Geophysical Research: Atmospheres*, 104(D22):27535–27543, November 1999.

[31] M. Kaufmann, C. Lehmann, L. Hoffmann, B. Funke, M. López-Puertas, C. von Savigny, and M. Riese. Chemical heating rates derived from SCIAMACHY vibrationally excited OH limb emission spectra. *Advances in Space Research*, 41:1914 – 1920, 2008. Record converted from VDB: 12.11.2012.

[32] U von Zahn, K. H Fricke, R Gerndt, and T Blix. Mesospheric temperatures and the OH layer height as derived from ground-based lidar and OH* spectrometry. *Journal of Atmospheric and Terrestrial Physics*, 49(7–8):863–869, July 1987.

[33] Jeng-Hwa Yee, G. Crowley, R. G. Roble, W. R. Skinner, M. D. Burrage, and P. B. Hays. Global simulations and observations of O(1s), O2(1Σ) and OH mesospheric nightglow emissions. *Journal of Geophysical Research: Space Physics*, 102(A9):19949–19968, September 1997.

[34] M. J. Lopez-Gonzalez, M. Garcia-Comas, E. Rodriguez, M. Lopez-Puertas, M. G. Shepherd, G. G. Shepherd, S. Sargoytchev, V. M. Aushev, S. M. Smith, M. G. Mlynczak, J. M. Russell, S. Brown, Y. M. Cho, and R. H. Wiens. Ground-based mesospheric temperatures at mid-latitude derived from O2 and OH airglow SATI data: Comparison with SABER measurements. *Journal of Atmospheric and Solar-Terrestrial Physics*, 69(17–18):2379–2390, December 2007.

[35] Official not webpage. `http://www.not.iac.es/`. Accessed: 2015-05-15.

[36] Notcam array overview. `http://www.not.iac.es/instruments/notcam/new-sci-arr.html`. Accessed: 2015-05-15.

[37] Notcam quality controle webpage. `http://www.not.iac.es/instruments/qc/notcamqcrrr.php`. Accessed: 2015-05-15.

[38] Official iraf webpage. `http://www.iraf.net`. Accessed: 2015-05-15.

[39] W. Pendleton, P. Espy, D. Baker, A. Steed, M. Fetrow, and K. Henriksen. Observation of oh meinel (7,4) p(n''=13) transitions in the night airglow. *Journal of Geophysical Research: Space Physics*, 94(A1):505–510, 1989.

[40] Bo-Cai Gao and Alexander F. H. Goetz. Column atmospheric water vapor and vegetation liquid water retrievals from airborne imaging spectrometer data. *Journal of Geophysical Research: Atmospheres*, 95(D4):3549–3564, 1990.

[41] F. Rademakers R. Brun. Root - an object oriented data analysis framework. *Nucl. Inst. & Meth. in Phys. Res. A*, pages 81–86, September 1996.

[42] *ROOT Reference Guide*. http://root.cern.ch/root/html/.

[43] Brian Gough, editor. *GNU Scientific Library Reference Manual - Third Edition*. Network Theory Ltd., s.l., 3rd revised edition edition edition, January 2009.

[44] Richard P. Brent. *Algorithms for Minimization Without Derivatives*. Dover Publications, Mineola, N.Y, 1993.

[45] Documentation of the brent algorithm from gsl. `http://www.gnu.org/software/gsl/manual/html_node/Minimization-Algorithms.html#Minimization-Algorithms`. Accessed: 2015-07-08.

[46] Thomas Williams, Colin Kelley, and many others. Gnuplot 4.4: an interactive plotting program. `http://gnuplot.sourceforge.net/`, March 2010.

[47] The MathWorks Inc. Matlab and statistics toolbox release 2014b. Natick, Massachusetts, United States.

[48] C. von Savigny, I. C. McDade, K.-U. Eichmann, and J. P. Burrows. On the dependence of the OH^* Meinel emission altitude on vibrational level: SCIAMACHY observations and model simulations. *Atmospheric Chemistry and Physics*, 12(18):8813–8828, 2012.

[49] Official eso webpage. `https://www.eso.org/sci/facilities/lpo.html`. Accessed: 2015-06-18.

[50] Xshooter instrument's characteristics. `https://www.eso.org/sci/facilities/paranal/instruments/xshooter/inst.html`. Accessed: 2015-06-18.

[51] G. Kvifte. Temperature measurements from {OH} bands. *Planetary and Space Science*, 5(2):153 – 157, 1961.

[52] R.P. Lowe, L.M. LeBlanc, and K.L. Gilbert. Windii/uars observation of twilight behaviour of the hydroxyl airglow, at mid-latitude equinox. *Journal of Atmospheric and Terrestrial Physics*, 58(16):1863 – 1869, 1996. Atmospheric Studies by Optical Methods.

[53] K. Nielsen, M.J. Taylor, R.E. Hibbins, and M.J. Jarvis. Climatology of short-period mesospheric gravity waves over Halley, Antarctica (76°S, 27°W). *Journal of Atmospheric and Solar-Terrestrial Physics*, 71(8–9):991 – 1000, 2009.

[54] Ndmc mission statement. `http://andromeda.caf.dlr.de/ndmc`. Accessed: 2015-07-21.

List of Abbreviations

NOT	Nordic Optical Telescope
NOTCam	Nordic Optical Telescope near-infrared Camera and spectrograph
NOTSA	Nordic Optical Telescope Scientific Association
IPCC	Intergovernmental Panel on Climate Change
CCMC	Community Coordinated Modelling Centre
NASA	National Aeronautics and Space Administration
CIRA	COSPAR International Reference Atmosphere
MSIS	Mass-Spectrometer-Incoherent-Scatter
HITRAN	High Resolution Transmission
GSL	Gnu Scientific Library
OH	Hydroxyl
MLT	Mesosphere and Lower Thermosphere
UT	Universal Time
NDF	Number Degrees of Freedom
NIR	Near Infrared

List of Tables

List of Figures